Non-Hydroxyl Radical Species Production during Dark Air Oxidation of Alluvial Soils

Elora Bourbon, Frédéric Averseng, Pierre Le Pape, Thierry Allard, Fulvia Baratelli, Fabrice Alliot, Alexandre Gélabert, Valentine Rollot, Elodie Guigon, Jessica Brest, et al.

Non-hydroxyl radical species production during dark air-oxidation of alluvial soils

Elora Bourbon[1,5], Frédéric Averseng[2], Pierre Le Pape[1], Thierry Allard[1], Fulvia Baratelli[3], Fabrice Alliot[3], Alexandre Gélabert[4], Valentine Rollot[4], Elodie Guigon[3], Jessica Brest[1], Sylvie Nélieu[5], Guillaume Morin[1]*

[1]*Institut de Minéralogie, de Physique des Matériaux et de Cosmochimie (IMPMC), UMR 7590, CNRS-Sorbonne Université, MNHN, IRD, 4 place Jussieu, 75252 Paris Cedex 05, France*

[2]*Laboratoire de Réactivité de Surface (LRS) UMR 7197, Sorbonne Université – CNRS, 4 place Jussieu, 75252 Paris Cedex 05, France*

[3]*Milieux Environnementaux, Transferts et Interactions dans les hydrosystèmes et les Sols (METIS), UMR 7619 Sorbonne Université, CNRS, EPHE, 4 place Jussieu, 75252 Paris Cedex 05, France.*

[4]*Institut de Physique du Globe de Paris, Sorbonne Paris Cité, Université Paris Diderot, UMR 7154 CNRS, 75005 Paris, France*

[5]*Ecologie fonctionnelle et écotoxicologie des agroécosystèmes (ECOSYS), UMR 1402, Université Paris-Saclay, INRAE, AgroParisTech, 91120 Palaiseau, France*

2nd revised version (R2) to be submitted to *ACS Earth and Space Chemistry*

*Corresponding Author: guillaume.morin@sorbonne-universite.fr

ABSTRACT

Natural environments subjected to hydrologically-driven redox fluctuations are regarded as propitious to contaminant degradation since they favor cyclic oxygenation of Fe(II)-minerals that produces oxidizing reactive species, such as the hydroxyl radical, $OH^{\bullet}$. However, the identity of these reactive species may vary as a function of physicochemical conditions and is still a matter of research. Here, using spin-trapping electron paramagnetic resonance (EPR) with 5,5-dimethyl-1-pyrroline *N*-oxide (DMPO) as spin trap, we show that a non-hydroxyl reactive species is produced in significant amount upon air-oxidation of alluvial soil suspensions (Seine River basin, France). Indeed, among the DMPO-$OH^{\bullet}$, DMPO-$CO_2^{\bullet-}$ and DMPO-alkyl$^{\bullet}$ adducts observed, the latter one dramatically raised when adding ethanol or, to a lesser extent, *tert*-butanol, especially with phosphate buffer. This result revealed a dominant non-hydroxyl species we interpret as Fe(IV) since it is known to oxidize alcohols into alkyl$^{\bullet}$ radicals and to be favored by phosphate ligands. With phosphate buffer and ethanol, the DMPO-alkyl$^{\bullet}$ production correlated with the initial reduced-state iron pool in the samples determined using Fe *K*-edge X-ray absorption spectroscopy (XAS). Fe(II)-phyllosilicates, and Fe(0) in one soil, and to a lesser extent vivianite, were the most significantly oxidized upon soil oxygenation, pyrite appearing less reactive. Hence, we show that a significant reactive species, differing from $OH^{\bullet}$, forms upon oxygenation of soil Fe(II)-minerals, especially in the presence of soil-sourced phosphate. Our results may thus call for further direct identification of this putative Fe(IV) species and for investigating its ability to degrade organic contaminants in natural environments.

KEYWORDS: alkyl$^{\bullet}$, $OH^{\bullet}$, $CO_2^{\bullet-}$, Fe(IV), phosphate, clays, EPR, XAS

48

49

50 **GRAPHICAL ABSTRACT (TOC)**

51

52

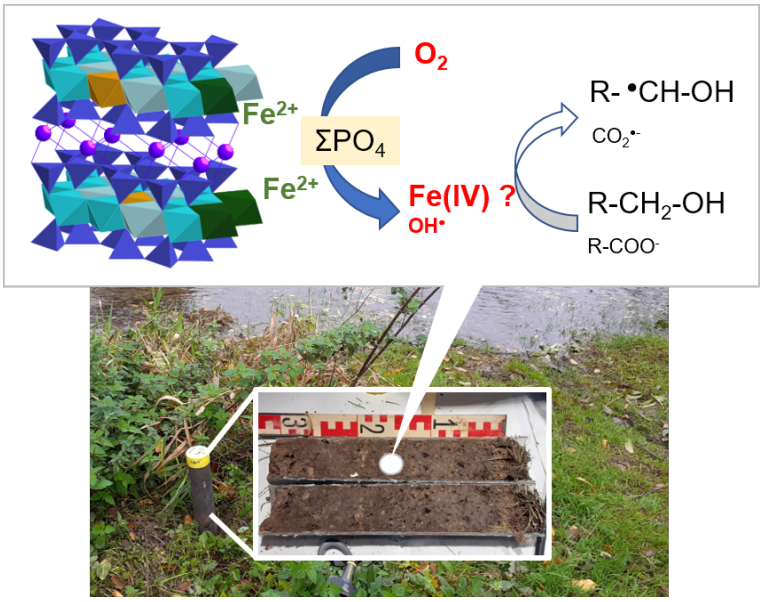

53
54
55

INTRODUCTION

A wide diversity of advanced oxidation processes has been the subject of intense research for the last decades in order to help designing efficient remediation processes for organic pollutants in water and soils[1–3]. Among recent developments, particular interest has been devoted to investigate Fenton-based processes using iron-bearing compounds as catalysts and airborne O_2 as oxidant, especially in order to promote eco-compatible routes favoring circumneutral pH and avoiding strong oxidants[4,5]. For instance, various organic compounds have been reported to be degraded upon oxygenation of iron-rich solid phases such as zero-valent iron[6], magnetite[7,8], FeS[9,10], pyrite[11] and clay minerals[12–14]. Moreover, some studies have provided promising results regarding the degradation of organic contaminants upon oxygenation of natural soils and sediments, in relation with the redox reactivity of Fe(II)-bearing soil components[15–17]. In these studies, organic contaminant degradation has been attributed to the oxidizing role of reactive oxygen species (ROS), particularly $OH^{\bullet}$, that have been reported to be produced upon oxygenation of reduced soils and sediments[17–23]. Some of these studies proposed that $OH^{\bullet}$ production could be related to oxidation of iron minerals[15–18] and organic matter[18,24–26]. Nevertheless, in aqueous media that are relevant to this literature, the actual formation of $OH^{\bullet}$ could be probed only using indirect approaches, due to the high reactivity and extremely short lifetime of this species (typically estimated to $\sim 10^{-9}$ s at 37°C in 1M linoleate [27]). Thus, $OH^{\bullet}$ scavengers have been used to investigate the role of this radical species in pollutant degradation[16]. More generally, the hydroxylation of specific aromatic molecules by $OH^{\bullet}$ has been rather used to obtain quantitative estimates of this short-lived species. In particular, the production rate of *p*-hydroxybenzoic acid (*p*-HBA) from benzoic acid (BA) has been often used to assess $OH^{\bullet}$ production. This method was first established by Zhou & Mopper[28] and has been now commonly used in various contexts including in soils and sediments oxygenation experiments[15,20,26,29,30]. Similarly, the conversion of terephthalic acid (TPA) into hydroxyterephthalic acid (hTPA) is another method that has been used to quantify $OH^{\bullet}$[18,19] upon oxygenation of soils. However, the specificity of aromatic hydroxylation methods, especially the ability of the BA/*p*-HBA method to selectively quantify

aqueous $OH^{\bullet}$ upon Fe(II)-mineral air-oxidation have been recently questioned[31]. In addition, the molecular-scale mechanisms of heterogeneous Fenton-like reaction using O_2 as the primary oxidant, remains an ongoing debate.

Besides, while it is commonly assumed that $OH^{\bullet}$ is produced under such oxygenation conditions, spin-trapping electronic paramagnetic resonance (EPR) spectroscopy studies have revealed a wider variety of radicals species that can be produced upon oxygenation of soils or sediments, including alkyl radicals that can be formed upon oxidation of natural organic matter by reactive oxygen species[32,33]. Moreover, pioneering and recent spin-trapping EPR studies have suggested that another reactive species, the ferryl ion $Fe(IV)=O^{2+}$, is formed upon oxygenation of Fe(II) at neutral and alkaline pH[34–36]. This was not confirmed by another indirect method involving the conversion of phenyl methyl/dimethyl sulfoxide (PMSO/DMSO) to phenyl methyl/dimeththyl sulfone (PMSO), which was not observed upon oxygenation of aqueous iron complexes[37] or magnetite at neutral pH[38], although this conversion is expected to occur in the presence of Fe(IV). In contrast in another study, the PMSO to $PMSO_2$ conversion was observed upon oxygenation of reduced smectites and rectorite[39]. Nevertheless, the selectivity of this latter method has been recently disputed[40]. Hence, although providing direct evidence for Fe(IV) in aqueous systems remains challenging[41–43], EPR studies have given clues for the formation of abundant non-hydroxyl species upon homogeneous and heterogeneous oxygenation of Fe(II), especially in the presence of ligands such as phosphate[34,36], which has been interpreted as possible ligand-promoted Fe(IV) formation[35].

Nevertheless, natural environments subjected to hydrological fluctuations are particularly regarded as propitious to such contaminant degradation processes since they may favor cyclic oxygenation of Fe(II)-minerals. Indeed, due to fluctuations of the redox boundary in riverbanks, alluvial soils or coastal areas sediments[23–25], ROS are expected to be produced during low-water periods from the oxidation of reduced-state iron substrates that may be regenerated via microbial reduction during high-water periods, thus contributing to ROS production at the next low-water period[23,33,44].

According to these previous findings, the mechanisms of ROS production in soils subjected to redox fluctuation thus deserve further research. The two main objective of this work were to better characterize the reactive species involved in the air-oxidation of natural soils in darkness at neutral pH, using spin-trapping EPR spectroscopy, and to evaluate the role of Fe-bearing phases in the reactive species production, using X-ray absorption spectroscopy (XAS) as a probe for Fe-speciation.

MATERIALS AND METHODS

All samples were handled in a JACOMEX® glovebox under N_2 atmosphere (O_2 < 2 ppm, as measured using a JACOMEX® electro-galvanic oxygen sensor) to avoid oxidation of the alluvial soil samples before oxygenation experiments. When required, O_2-free deionized water (18.2 mΩ.cm, Millipore® Milli-Q system) was prepared by bubbling N_2 gas at 75°C for 50 minutes, ensuring dissolved O_2 concentration in the 10^{-5} mg.L^{-1} range[45]. All experiments presented were conducted at room temperature except XAS analyses that were conducted at cryogenic temperature to limit beam-damage.

Alluvial soils sampling and characterization procedures. Alluvial soils were collected from two different locations (**Figure S1**, top). Two soil cores were collected in the Orgeval watershed, on the banks of the Avenelles river, on the edge of a cropped field (CRD3) and of a meadow (CRG1). A third alluvial soil core was collected in the Seine riverbank upstream from the Bassée alluvial plain (T1S1). At the Avenelles site, we used a PVC tube and a rubber hammer for coring. A manual steel corer with an inner PVC tube and a rubber hammer were used to core the muddy soil at the T1S1 site. The soils cores of about 30 cm length were immediately sealed in their PVC tube with taped plastic stoppers in order to limit contact with atmosphere and were transported in a passive cool box (≤ 5°C) to the IMPMC laboratory within 24 hours. The cores within their PVC tubes were cut transversally in the glovebox and half-cores were subdivided into subsamples as a function of depth, according to

131 the difference of colors and textures of the horizons. Subsamples were then dried under vacuum in a
132 desiccator within the glovebox.

133 Major elements concentrations in the dry soils samples were determined by Inductively Coupled
134 Plasma - Optical Emission Spectrometry (ICP-OES), at SARM-CRPG (Nancy, France) after alkaline
135 fusion and acid digestion (**Table 1**). Full chemical compositions are reported in **Table S1**. Total
136 carbon, total organic carbon (TOC), and total inorganic carbon (TIC) calculated by subtraction (**Table**
137 **1**), were determined in dried samples in three replicates by pyrolysis and element analysis using a
138 Vario Isotope Select element analyzer (Elementar, Lyon, France) at ECOSYS, INRAE. Prior to the
139 organic carbon measurements, inorganic carbon was eliminated from soils by acidic fumigation using
140 HCl[46].

141 For two selected samples, CRD3 20-30 cm and T1S1 0-10 cm, dissolved organic carbon (DOC)
142 was measured in the filtered suspension after air-oxidation (please see next section for oxidation
143 protocol) using a total organic carbon analyzer TOC-5050A (Shimadzu, Marne-La-Vallée, France).
144 Uncertainties were estimated from two independent experiments. Phosphate concentration was
145 measured by the molybdenum blue reaction with orthophosphate, by colorimetry at 710 nm,[47] in the
146 filtered suspension before air-oxidation and uncertainties were estimated from triplicate experiments.

147 The mineralogy of the dried soil subsamples was determined using powder X-ray diffraction
148 (XRD) and Scanning Electron Microscopy coupled to Energy Dispersive X-ray analysis (SEM-
149 EDX). XRD data were collected using a PANalytical® Xpert Pro diffractometer in Bragg-Brentano
150 geometry with Co-*K*α radiation, for 2h between 2 and 80° 2θ-range in a continuous mode. For this
151 purpose, soil samples were ground in the anoxic glove-box in an agate mortar in mixture with ethanol
152 and were deposited on a zero-background silicon wafer before being placed into an anoxic chamber
153 with Kapton® window during the XRD measurements. Mineral phases were identified using the
154 HighScore Plus® software and the PDF-2 database (**Table 1**).

155 For scanning electron microscopy coupled to energy dispersive X-ray (SEM-EDX) spectroscopy
156 analyses, ~50 µm thick soil thin-sections were prepared on glass slides from soil powder embedded

157 in Epoxy resin. SEM observations were performed on a Zeiss Ultra55 SEM equipped with a FEG-
158 Schottky electronic source operating at 15 kV and with a Bruker™ Si-drift detector for EDX. Semi-
159 quantitative elemental analysis was performed on EDX spectra using the Esprit1.9® using a spectra
160 database for standard materials (**Figure 1**).

161 **Air-oxidation procedure.** To avoid any photo-activation from natural light, the air-oxidation
162 experiments were conducted within amber glass flasks. For all samples of the CRD3, CRG1 and T1S1
163 soil cores, suspensions were prepared in an anoxic glove box. For this purpose, 100 mg of dried
164 sample were mixed with 350 µL phosphate buffer 1 M pH 7 (prepared from anhydrous NaH_2PO_4 and
165 Na_2HPO_4 salts), 16 µL of 99.98% absolute ethanol, 160 µL of O_2-free deionized water, and then 300
166 µL of DMPO 0.1 M (n° CAS: 3317-61-1; ≥ 98.0 % for EPR-spectroscopy, Sigma-Aldrich®). Final
167 concentrations in the mixture are 0.036 M, 0.42 M, 0.33 M for DMPO, phosphate and ethanol
168 respectively. The suspensions were left equilibrating overnight before adding DMPO and sealing the
169 flasks with butyl rubber stoppers. Air-oxidation was performed outside from the glove box, by
170 injecting 200 mL of air over a two minutes period of time using a 50 mL syringe and needle through
171 the butyl rubber stopper. The suspension is 60±5% saturated with O_2 after this 2 min air bubbling as
172 determined with a WTW® 3630 IDS FDO Check probe for dissolved oxygen. The flask was then
173 shaken for ten seconds and the liquid phase was extracted with a 5 mL syringe and needle and was
174 then filtered through 0.2 µm nylon filters before being transferred in an EPR liquid flat-cell for
175 analysis. Besides, a control experiment without solid was also carried out in the same conditions and
176 is referred to as blank.

177 In order to better decipher among various possible reactive species, specific experiments were
178 conducted on the CRD3 20-30 cm and T1S1 0-10 cm samples, with or without adding 16 µL of the
179 $OH^{\bullet}$ scavenger, i.e. either ethanol (99.98%) or *tert*-butanol (99%). In addition, to assess the possible
180 effects of ligands, the air-oxidation experiments were conducted with or without phosphate buffer,
181 then replacing it by O_2-free deionized water. Removing the buffer did not significantly affect the pH

of the suspensions upon oxygenation since they were already buffered at pH 7.0-7.3 by the soil alkalinity and dropped to 6.7-6.8 after oxidation.

Spin-trapping Electron Paramagnetic Resonance (EPR). Immediately after the air-oxidation, shaking and filtration steps, an EPR spectrum was acquired every 5 min over a one-hour period, with the beginning of air-bubbling as the initial time reference (t = 0 min). For these measurements, X-band EPR spectra were acquired at room temperature at the IMPMC laboratory over the 0.3460 – 0.3560 Tesla magnetic field-range on a Bruker EMXplus™ EPR spectrometer, or at the LRS laboratory, over the 0.33204−0.34204 Tesla magnetic field-range on a JEOL® FA-300 spectrometer (**Figure S2**). Acquisition parameters are detailed in Supporting Information Section S1.

As in Morin et al. (2023)[36], EPR spectra were least-squares fit using the EPRPLP code[48] in order to extract EPR parameters of the DMPO-radical adducts (**Table 2; Figure 2**) and scale factors proportional to the abundance of every adduct as a function of time. Typical time course series of EPR spectra collected for this spin-trapping kinetic EPR analysis are displayed in **Figure S3**. For all experiments, the time-course evolution of the scale factor for each adduct was fit by a combination of two first order kinetic laws, representing the adduct production and decay, which can be expressed as follows for a given DMPO-radical$^{\bullet}$ adduct (**Figures S4 and S5** ; **Table S2** and **Table 3)**:

$$[\text{DMPO-radical}^{\bullet}](t) = [\text{DMPO-radical}^{\bullet}]_{max} \cdot \frac{k_{prod}}{(k_{decay} - k_{prod})} \cdot \left(e^{-k_{prod} \cdot t} - e^{-k_{decay} \cdot t}\right) \quad (1)$$

where k_{prod} and k_{decay} are rate constants and $[\text{DMPO-radical}^{\bullet}]_{max}$ is the calculated maximum EPR intensity. This latter parameter was then used as an estimate of the amount of radical species produced in our air-oxidation experiments (**Table S2; Figures S6 and S7**). Triplicate experiments were especially conducted with phosphate buffer and EtOH for all samples (**Figure S8**; **Table 3**). As previously observed in a previous study[36] upon air-oxidation of pure iron substrates, a short radical production phase is observed (k_{prod}) before decay (k_{decay}) indicating that radicals are still produced in the filtered supernatant after the 2 min bubbling. This effect is related to the contribution of aqueous

208 Fe(II) species oxidation to radical production after filtration, in addition to surface Fe(II) species
209 oxidized before filtration[31,36].

210 **X-ray Absorption Spectroscopy (XAS).** Iron *K*-edge X-ray Absorption Near Edge Structure
211 (XANES) and Extended X-ray Absorption Fine Structure (EXAFS) spectroscopy data were collected
212 on the soil core samples before and after the same 2 min air-oxidation protocol as that used for EPR
213 analyses, but without DMPO. Following the bubbling step, samples were centrifuged for 20 seconds
214 before being vacuum-dried into the anoxic glovebox. In the glove box, the samples were ground in
215 agate mortar, weighted to ~30 mg to optimize edge-jump vs. total absorbance, pressed as pure pellets,
216 sealed under Kapton® tape and mounted on samples holders. Those were then sealed within glass
217 vials closed with butyl rubber stoppers and brought to the synchrotron beamline glove box. The
218 sample holders were exposed to air for less than 20 seconds before being placed into the liquid
219 nitrogen cryostat sample chamber that was then pumped down to ~10^{-6} bar and cooled. The data on
220 the CRD3 and T1S1 samples were collected at 80K in transmission detection mode using ionization
221 chambers on the bending-magnet XAFS beamline at the ELETTRA synchrotron (Trieste, Italy).
222 Energy was selected using a Si(111) double-crystal monochromator detuned for 30% in order to avoid
223 the 3rd order harmonic. The data on the CRG1 samples were collected at 30K on the undulator LUCIA
224 beamline at the SOLEIL synchrotron (Saint-Aubin, France) using a Si(111) double-crystal
225 monochromator, and harmonic rejection mirrors. On this beamline, transmission and fluorescence
226 (Si-drift detector) detection mode data were used for EXAFS and XANES, respectively. Energy was
227 calibrated using a Fe foil analyzed in double-transmission setup, setting the first inflection point of
228 the Fe *K*-edge at 7112 eV. Either two or three spectra were merged, normalized, background-
229 subtracted, and deglitched if necessary, using the Athena software[49].

230 A Principal Component Analysis (PCA) and Target Transform (TT) analysis (**Figure S9-S11**;
231 **Table S3**), followed by Linear combination fit (LCF) **(Figures 3 and 4; Table 4)** was performed to
232 assess iron speciation in the soil samples, before and after air-oxidation. PCA-TT was performed
233 using the SIXPack software[50], whereas XANES and EXAFS LCF was performed with a home-built

Fortran 90 code based on a Levenberg-Marquardt minimization algorithm used in previous studies[51–55].

In this latter software, fit quality for XANES LCF is estimated with a R-factor, $R_f = \Sigma [\mu_{exp}-\mu_{fit}]^2 / \Sigma \mu_{exp}^2$, where μ is the normalized absorbance, and with a reduced chi-square, $Chi^2_R = N/(N-N_p) [\mu_{exp}-\mu_{fit}]^2 / \Sigma \mu_{exp}^2$, where N_p is the number of fitting components and N is the number of independent parameters corresponding to the energy range divided by the natural width of the Fe levels[56]. The uncertainty on each fitting parameter p was estimated to 99.7% confidence (3σ) as $3\sqrt{(var(p).Chi^2_R}$, where var(p) is the variance of parameter p returned by the Levenberg-Marquardt routine for the lowest Chi_2^R value. The fit quality of EXAFS LCF was estimated by a reduced chi-square parameter $Chi^2_R, = N/[(N-N_p).n.\varepsilon^2] \sum[k^3\chi(k)_{exp} - k^3\chi(k)_{fit}]^2$, with $N = (2\Delta k\Delta R)/\pi$, the number of independent parameters, Np the number of free fitting parameters, n the number of data points, and ε the root mean square of the data noise. This latter value was estimated as the Fourier back-transform of the data in the 15–25 Å R-range, following a method modified after Ravel and Newville[43]. The uncertainty on EXAFS fitting parameters was estimated to 95% confidence (2σ) by $2\sqrt{(var(p).Chi^2_R}$, where var(p) is the variance of parameter p returned by the Levenberg-Marquardt routine for the lowest Chi^2_R value. Fitting components were selected from our database using the results of TT analysis (**Table S3**) and were further screened by requiring uncertainties returned from the LCF procedure to be lower than the refined parameter values (**Table 4**). Applying this method, a consistent set of six fitting components, i.e. Fe(0), pyrite, vivianite, biotite, illite and goethite, was found to fit both XANES and EXAFS spectra of our whole set of soil cores samples, before and after air-oxidation. Calculated uncertainties revealed that vivianite and pyrite minor components, although observed by SEM, were significant in XANES fitting but not in EXAFS fitting **(Figure 4; Table 4)**. In contrast, Fe(0) was required to fit both the XANES and EXAFS data of CRD3 samples (**Figure S12**; **Table S4**). This component may be attributed to steel or other metallic particles, some of which being identified by SEM-EDX observations (**Figure 1**). We infer that they could originate from incident anthropogenic inputs in the studied cropped fields, due for instance to soil tilling.

Thanks to lower uncertainties and reliable sum-of-component criteria, XANES spectroscopy was more accurate at determining Fe redox state than EXAFS and was then used to evaluate the "reduced-state iron" pool, calculated as the sum of Fe(0) and Fe(II) **(Table 4)**. This observation obviously results from the well-known sensitivity of the energy position of the Fe *K*-edge to oxidation state and first-ligands, which allows accurate determination of Fe oxidation state in complex natural samples using XANES LCF, provided that appropriate model compounds are available[53,55,57–59].

RESULTS AND DISCUSSION

Chemical and mineralogical characterization of the alluvial soils

Major minerals determined by XRD analysis, i.e. quartz, feldspars, calcite and clay minerals (**Table 1; Figure S1**) were in qualitative agreement with ICP-OES data (**Table 1 and S1**). Hence, the samples from the Seine site (T1S1) were found to be more calcic than the siliceous soils from the Avenelles site (CRD3 and CRG1).

Table 1. Selected chemical and mineralogical data on the studied soil core samples, as determined by ICP-OES (Fe and S concentrations refer to total concentrations of these elements), carbon analyser (TOC, TIC), powder XRD (Qz: Quartz; Cal: Calcite; Feld: Feldspar; Clay: phyllosilicates; **Figure S1**) and SEM-EDX (Viv: vivianite, Py: pyrite; Fe-Ox: iron oxyhydroxides; OM: organic matter; Fe(0): metallic iron (**Figure 1**). Relative analytical uncertainties are ±10%, ±20% and ±15% for Fe, S and P, respectively. Uncertainties (3σ) on last digit are given under bracket for triplicate measurements of TOC and TIC.

Sample	Fe (wt%)	S (wt%)	P (wt%)	TOC (wt%)	TIC (wt%)	Major minerals	Fe-bearing phases
CRD3 0-3 cm	0.67	0.03	< 0.044	1.4(2)	0.2(1)	Qz, Cal, Feld, Clays	Clays, Fe-Ox, Fe(0)
CRD3 3-10 cm	0.97	0.04	< 0.044	2.06(6)	0.12(1)		
CRD3 10-20 cm	0.92	0.05	< 0.044	1.6(1)	0.3(2)		
CRD3 20-30 cm	1.02	0.04	< 0.044	4.2(1)	0.2(1)		
CRG1 8-14 cm	1.09	0.06	0.048	3.8(2)	0.3(2)	Qz, Cal, Feld, Clays	Clays, Fe-Ox
CRG1 14-21 cm	0.79	0.04	< 0.044	2.2(4)	0.4(3)		
CRG1 21-28 cm	1.23	0.07	0.057	3.9(1)	0.2(2)		
CRG1 28-35 cm	1.18	0.07	0.052	5.4(3)	0.3(3)		
T1S1 0-10 cm	1.58	0.10	0.096	4.2(7)	5.7(7)	Cal, Qz, Clays	Clays, Fe-Ox, Viv, Py, OM
T1S1 10-15 cm	1.59	0.07	0.096	4.1(7)	5.7(8)		
T1S1 15-24 cm	1.54	0.08	0.100	4(1)	6(1)		
T1S1 24-30 cm	0.92	0.07	0.061	2.2(2)	7.9(3)		

Complementary information on minor Fe-bearing phases below XRD detection limit was provided by SEM-EDX analysis (**Figure 1**). Fe-bearing phyllosilicates and iron-oxyhydroxides were identified as Fe-bearing phases in the CRD3 and CRG1 soil cores (**Figure 1**; **Table 1**) and metallic iron particles were observed in the former core (**Figure 1e**). In the T1S1 soils, Fe-bearing phyllosilicates and iron-oxyhydroxides were also observed, as well as iron associated to organic matter (**Figure 1d**), framboidal pyrite (FeS_2) (**Figure 1b**) and vivianite ($Fe_3(PO_4)_2 \cdot 8H_2O$) (**Figure 1c**).

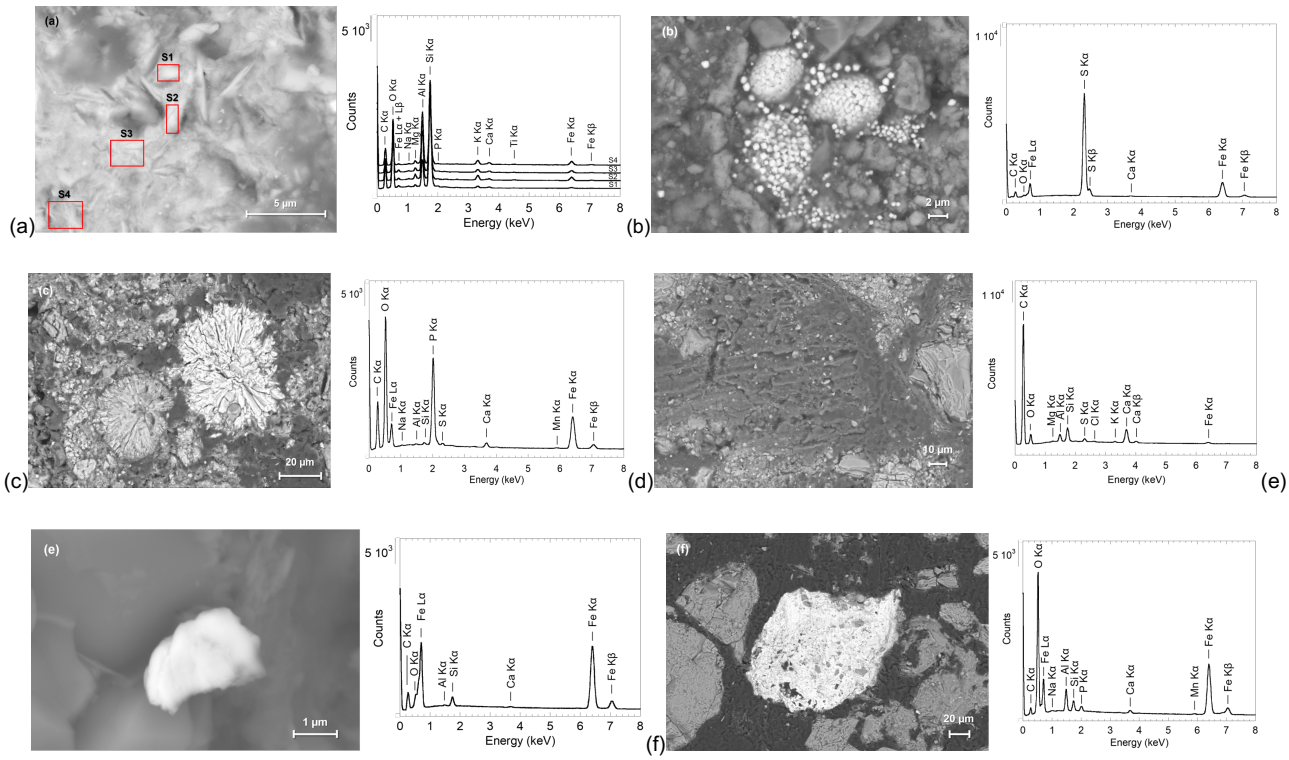

Figure 1. SEM images in backscattering mode (left) and corresponding EDX spectra (right) (a) phyllosilicate aggregate in CRD3 0-3 cm sample with spectra corresponding to the red tags, (b) framboidal pyrites in T1S1 24-30 cm sample (Fe/S = 0.50 ± 0.05 mol/mol) (c) vivianite grain in T1S1 24-30 cm sample (Fe/P = 1.40 ± 0.05 mol/mol) (d) organic matter aggregate in T1S1 24-30 cm sample (Fe/C = 0.08 ± 0.01 mol/mol) (e) metalli iron grain in CRD3 20-30 cm sample (f) iron oxyhydroxide in CRD3 0-3 cm sample.

Radical species produced upon air-oxidation of the alluvial soils. Three DMPO adducts were produced upon air-oxidation of the soil suspensions particularly in the absence of alcohol and phosphate buffer, and were observed by EPR in the filtered soil suspensions, as shown in **Figure 2a**.

The first signal is the DMPO-OH• adduct, characterized by its quadruplet spectrum[60,61] (**Table 2**). Accordingly, DMPO is known as an efficient spin trap for the hydroxyl radical OH• and the DMPO-OH• adduct has been previously detected using EPR upon oxygenation of soils[15,20] and of Fe(II)-bearing substrates such as FeS[9]. However, DMPO-OH• can be also formed by decomposition of DMPO-$O_2^{\bullet-}$ with typically a few percent of this adduct being transformed into DMPO-OH• after a few minutes[62]. Such origin for DMPO-OH• cannot be excluded in our experiments since the half-life of the DMPO-$O_2^{\bullet-}$ adduct is as short as 1 or 2 min, and even shorter in the presence of Fe^{2+}[62,63]. This adduct might then be overlooked by our first EPR spectrum that is taken at 5 min after the beginning of the oxygenation.

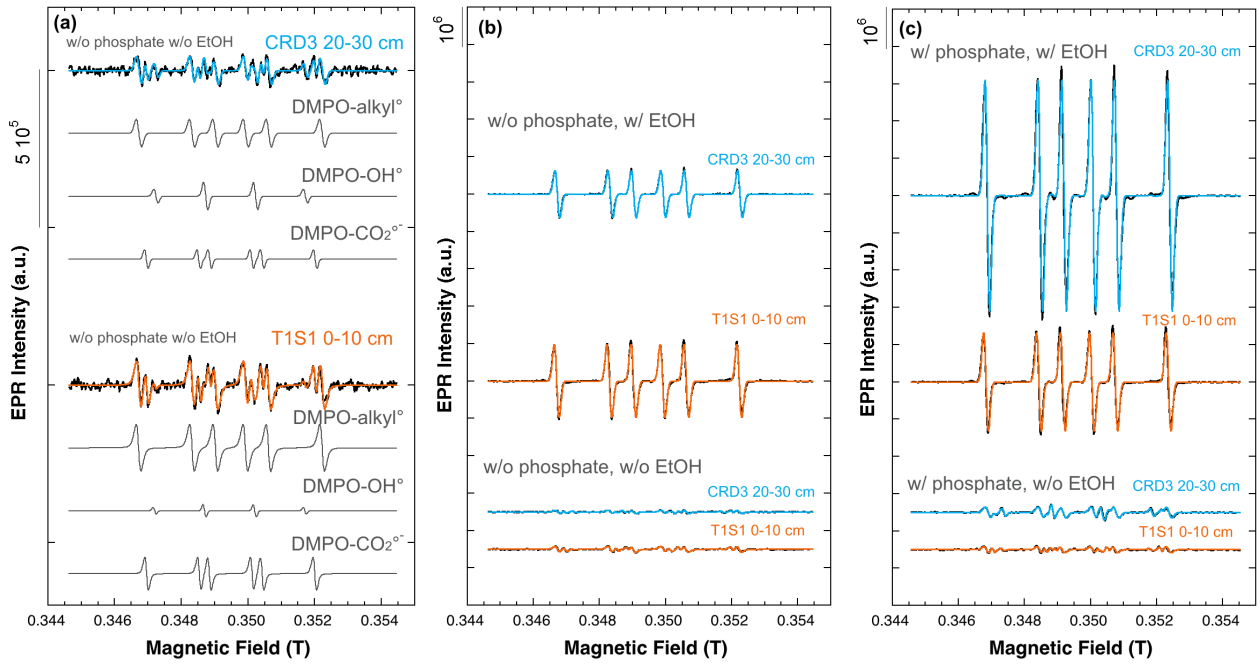

Figure 2. EPR spectra taken at time 26 ± 2 min after the start of 2 min air-oxidation of the CRD3 20-30 cm or T1S1 0-10 cm samples suspensions. (a) without phosphate buffer and without EtOH added. Experimental (black) and fitting curves (blue or orange) are displayed together with weighted theoretical fitting components: DMPO-alkyl•, DMPO-OH• and DMPO-$CO_2^{\bullet-}$ adducts. (b) Without phosphate buffer and without or with EtOH added. (c) With phosphate buffer and with or without EtOH added. EPR parameters of the adducts are reported in **Table 2**.

Nevertheless, even though the hydroxyl radical could be directly produced by oxygenation of Fe(II)-minerals at neutral pH, the intensity of DMPO-OH• EPR signal in our study, as well as in previous reports, was found to be close to the background signal[9,15,20]. In contrast, based on aromatic

hydroxylation methods such as BA/*p*-HBA conversion, $OH^{\bullet}$ has been assumed to be generated upon oxygenation of soils and sediments[17–23].

The second signal is a sextet with hyperfine parameters (**Table 2**) matching those of DMPO adducts of alkyl radicals ($RCH^{\bullet}R'$) or hydroxyalkyl radicals ($RCH^{\bullet}OH$) with R being an alkane or a H atom[61], which we will both refer to as DMPO-$alkyl^{\bullet}$ adduct thereafter. Such adduct is typically observed when a ROS scavenger, especially an alcohol, is present and reacts with the ROS before being trapped by DMPO[62]. Hence, $OH^{\bullet}$ scavengers such as methanol, ethanol or DMSO are used to distinguish genuine DMPO-$OH^{\bullet}$ from the same adduct resulting from the decomposition of DMPO-$O_2^{\bullet-}$, since the superoxide radical $O_2^{\bullet-}$ is not scavenged by alcohols nor DMSO[60,62]. In our experiments, one may infer that the DMPO-$alkyl^{\bullet}$ formation results from the scavenging of reactive species by alkyl groups associated to dissolved organic matter in our soil suspensions (**Table 1**), and their subsequent trapping by DMPO. Similar signal was indeed reported in the past upon oxygenation of sediments[15].

Table 2. EPR parameters of DMPO adducts of the hydroxyl radical (DMPO-$OH^{\bullet}$), carbon dioxide anion radical (DMPO-$CO_2^{\bullet-}$), hydroxyethyl radical (DMPO-$EtOH^{\bullet}$) and hydroxy*tert*-butyl radical (DMPO-t-$BuOH^{\bullet}$), determined from the fitting of soil samples suspension data. Parameters include the g factor of the (S=1/2) center and its hyperfine coupling constants to hydrogen (A_H) and nitrogen (A_N) neighbors.

		This study		*Buettner (1987)*[61] *	
Adduct	*g*	A_H (cm^{-1}) A_H (Gauss)	A_N (cm^{-1}) A_N (Gauss)	A_H (cm^{-1}) A_H (Gauss)	A_N (cm^{-1}) A_N (Gauss)
DMPO-$OH^{\bullet}$	2.0055(2)	0.00138(6) 14.7(7)	0.00141(6) 15.1(7)	0.00140(3) 15.0(3)	0.00140(3) 15.0(3)
DMPO-$CO_2^{\bullet-}$	2.0054(2)	0.00177(4) 18.9(4)	0.00149(2) 15.9(2)	0.00175(5) 18.7(5)	0.00146(4) 15.6(4)
DMPO-$alkyl^{\bullet}$	2.0054(1)	0.00217(4) 23.2(4)	0.00150(1) 16.0(1)	0.0022(2) 23.5(20)	0.00149(8) 15.9(8)

* Mean values of hyperfine constants reported in Buettner (1987)[61] converted in cm^{-1} unit using either g = 2.0054 or *g*-value reported therein. Only the values measured in water as solvent were kept for this calculation.

A third radical was observed, whose hyperfine constants matched those of DMPO-$CO_2^{\bullet-}$ adducts[60,61] (**Table 2**). The carbon anion radical $CO_2^{\bullet-}$ has been reported to be produced in the presence of formate $HCOO^-$ upon oxygenation of iron-bearing asbestos[64]. This radical was also detected in a Fe(II)-EDTA/H_2O_2 system at pH 7.4 in the presence of formate[65]. More recently, it has been reported $CO_2^{\bullet-}$ formation upon photo-oxidation of formate[66]. Besides, $CO_2^{\bullet-}$ was recently detected upon Cr(VI) reduction in wastewaters[67]. According to these previous reports, the $CO_2^{\bullet-}$ radical that formed upon oxygenation of our soils suspension could likely result from the oxidation of carboxylate compounds that necessarily originated from soil-sourced organic matter.

As shown in **Figure 2a**, the three DMPO adducts of $OH^{\bullet}$, alkyl$^{\bullet}$ and $CO_2^{\bullet-}$ were observed upon air-oxidation of alluvial soils samples from both sites, but with a higher intensity of alkyl$^{\bullet}$ and $CO_2^{\bullet-}$ radicals for the T1S1 sample than for the CRD3 sample. Since we infer that these two radicals may be generated through ROS scavenging by alkyl and carboxylate groups from dissolved organic matter, the more than two-fold higher amount of DOC in the filtered suspension after oxygenation of the T1S1 0-10 cm sample (150±40 $mg.L^{-1}$) compared to the CRD3 20-30 cm sample (65±20 $mg.L^{-1}$) could be invoked to explain this difference in radical production.

Effect of radical scavengers and phosphate. EtOH used as scavenger is expected to convert $OH^{\bullet}$ into the α-hydroxyethyl radical, $EtOH^{\bullet}$ and forms a DMPO-hydroxyethyl$^{\bullet}$ adduct with a sextet EPR spectrum, typical of the DMPO-alkyl$^{\bullet}$ adducts[62]. It can be then distinguished from the quadruplet spectrum of a DMPO-$OH^{\bullet}$ adduct that could have potentially resulted from the decomposition of DMPO-$O_2^{\bullet-}$[62]. In our experiments conducted in the absence of phosphate buffer, the addition of EtOH lead to a significant decrease of the DMPO-$OH^{\bullet}$ signal (**Figure 2b and S6**), suggesting that the major fraction of the DMPO-$OH^{\bullet}$ observed in the absence of both EtOH and phosphate buffer was related to the production of $OH^{\bullet}$ upon air-oxidation of the soil samples. Since $OH^{\bullet}$ is converted into alkyl$^{\bullet}$ in the presence of EtOH, the amount of DMPO-alkyl$^{\bullet}$ adduct would be expected to be in the same range as that of the DMPO-$OH^{\bullet}$ adduct observed in the absence of EtOH, as observed in Fenton-like

oxidation experiments performed with H_2O_2[36]. On the contrary, addition of EtOH led to a significant increase of the DMPO-alkyl$^\bullet$ sextet signal that was found about 50-fold higher than the DMPO-OH$^\bullet$ observed without EtOH (**Figure 2b** and **S6**, **Table S2**). Importantly, this strong DMPO-alkyl$^\bullet$ signal observed in the presence of added EtOH (**Figure 2b**) indicates that another non-hydroxyl species is produced by air-oxidation of our soil samples and that it is able to oxidize EtOH into EtOH$^\bullet$. More precisely, the relative proportions of this non-hydroxyl species and of the hydroxyl radical can be estimated, as shown in **Figure S6**, from the amounts of DMPO-OH$^\bullet$ and DMPO-alkyl$^\bullet$ adducts determined from our spin-trapping EPR kinetic analysis (**Table S2)**, the trapping rate constants of OH$^\bullet$ by DMPO[60] and EtOH[68] and the known concentrations of DMPO, EtOH and DOC in our soil suspensions. This estimation indicated that ~87 and ~99% of the DMPO-alkyl$^\bullet$ adduct signal is due to EtOH oxidation by a non-hydroxyl species upon air-oxidation of the CRD3 20-30 cm and T1S1 0-10cm soil suspensions, respectively, in the presence of EtOH. In other words, the relative proportion of non-hydroxyl species over hydroxyl species is estimated to 86 and 91% for the CRD3 20-30 cm and T1S1 0-10cm soil suspensions, respectively, in these conditions **(Figure S6)**. Previous evidences for the formation of a non-hydroxyl species air-oxidation of aqueous Fe(II) species[34,35] and Fe(II)-mineral phases[36] at near neutral pH have been reported from EPR spin-trapping analyses. In these former studies, the authors proposed that the main reactive species produced in such conditions may be a high-valent state of iron, the ferryl ion $Fe^{IV}O^{2+}$, since this species is known to oxidize EtOH into EtOH$^\bullet$ through hydrogen abstraction[4,65,69,70]. Indeed, the ferryl ion has been proposed as a possible product of Fe(II) oxidation by H_2O_2 in Fenton-like systems especially at neutral pH[65,71–76] and has been also proposed to form upon oxygenation of Fe(II)[34,35,77] and zero-valent iron[4,78]. Based on these findings, we hypothesize that, in our air-oxidation experiments in the presence of EtOH, the hydroxyethyl radical EtOH$^\bullet$ could have mainly formed from the following reactions[36,70] (**Figure 2b**):

$$Fe^{2+} + ½\ O_2 \Leftrightarrow Fe^{IV}O^{2+} \quad (2)$$

$$Fe^{IV}O^{2+} + EtOH \Leftrightarrow Fe^{III}(OH)^{2+} + EtOH^\bullet \quad (3)$$

while in the absence of EtOH, the low amount of observed alkyl radicals could have resulted from the oxidation of soils-sourced natural organic matter by both $OH^{\bullet}$ and Fe(IV) (**Figure 2a**):

$$OH^{\bullet} + alkyl_{soil\text{-}organic\text{-}matter} \Leftrightarrow H_2O + alkyl^{\bullet} \quad (4)$$

$$Fe^{IV}O^{2+} + alkyl_{soil\text{-}organic\text{-}matter} \Leftrightarrow Fe^{III}(OH)^{2+} + alkyl^{\bullet} \quad (5)$$

More detailed hypotheses on the mechanisms possibly underlying reaction (2) are especially reported in previous studies[4,32] and references therein. In the present study, support for this non-hydroxyl species is further provided by the results of air-oxidation experiments conducted in the presence of our concentrated phosphate buffer at pH 7 (**Figure 2c** and **S5**). Without ethanol, the overall EPR signal remained low but a slight increase could be observed compared to the experiments without phosphate buffer (**Figure 2b)**, especially for the CRD3 20-30 cm (**Figure S6**). In the presence of ethanol, addition of the phosphate buffer lead to a greater increase of the DMPO-alkyl$^{\bullet}$ adduct signal (**Figure 2c, S4a and S6**) than in the non-added phosphate experiments (**Figure 2b, S5a and S6**), especially for the CRD3 20-30 cm sample, indicating that phosphate favored the formation of the putative Fe(IV) species. More precisely, the amount of non-hydroxyl species, interpreted as Fe(IV), increased by factors of ~4 and ~2 for the CRD3 20-30 cm and T1S1 0-10 cm samples, respectively, when adding the phosphate buffer in the presence of EtOH (**Figure S6**). Furthermore, the relative proportion of putative Fe(IV) over hydroxyl radical species is estimated to 79 and 92% for the CRD3 20-30 cm and T1S1 0-10 cm soil suspensions, respectively, in the presence of added EtOH and phosphate buffer (**Figure S6**). Such effect of phosphate has been documented in previous studies[34–36] and is thought to be another hint pointing toward Fe(IV). Moreover, other specific iron complexing agents, such as EDTA, have been reported to favor the Fe(IV) pathway over the $OH^{\bullet}$ pathway at neutral pH, both in Fenton systems[65,72,73,79] and in oxygenation experiments[34–36]. Hence, the increase in alkyl$^{\bullet}$ radicals production observed in the presence of phosphate buffer (**Figure 2c** and **S6**) is consistent with the reported ability of phosphate to favor the formation of Fe(IV) over $OH^{\bullet}$ upon oxygenation at neutral pH[34–36]. Addition of ethanol in our EPR-spin trapping experiments is then thought to reveal Fe(IV) through the formation of the DMPO-alkyl$^{\bullet}$ adduct, due to the known

ability of this species to abstract an hydrogen atom to ethanol[4,65,69,70], leading to an EtOH• radical[34,36,62]. Moreover, according to the excess of DMPO over DOC in our experiments, the higher amount of DMPO-alkyl• adduct than DMPO-OH• in the absence of ethanol (**Figure 2a**, **S4a**, and **S5a**) suggests that a significant fraction of the soil-derived dissolved organic molecules may be oxidized rather by Fe(IV)[69] than by OH• to form alkyl• radicals. Accordingly, owing to DOC concentrations measured in our soil suspensions, i.e., 65±20 and 150±40 mg.L^{-1} for the T1S1 0-10 cm and CRD3 20-30 cm samples, respectively, the relative proportion of non-hydroxyl species largely exceeds that of hydroxyl radical in the absence of EtOH as estimated in **Figure S6.**

Interestingly, the effect of added ethanol and phosphate buffer on the production of DMPO-alkyl• varied among the two selected soil samples studied (**Figure 2b, 2c, S4, S5 and S6**), which suggests that soil-derived aqueous species present in the soil suspensions, specifically DOC and phosphate, may have interfered in the putative production of Fe(IV) during air-oxidation. Indeed, the stronger DMPO-alkyl• signal observed in T1S1 0-10 cm than in CRD3 20-30 cm, in the absence of phosphate buffer (**Figure 2a, 2b and S4a**; **Table S2**), could be explained by both the higher dissolved phosphate and higher dissolved organic carbon concentrations in the former sample suspension (2.1±0.1 mg.L^{-1} P as phosphate and 150±40 mg.L^{-1} DOC) than in the latter (1.2±0.4 mg.L^{-1} P as phosphate and 65±20 mg.L^{-1} DOC). Furthermore, assuming that CRD3 20-30 cm sample is more sensitive to air-oxidation than the T1S1 0-10 cm one, as it will be shown in the next section, the lower concentration of soil-sourced phosphate in CRD3 20-30 cm could help explaining why the addition of phosphate buffer has a larger effect on Fe(IV) production for this sample than for the T1S1 0-10 cm one, with and without EtOH (**Figure 2c**, **S5a and S6; Table S2**).

A supplementary result supporting the formation of Fe(IV), especially in the presence of phosphate buffer, is given by using *tert*-butanol (t-BuOH) instead of ethanol as radical scavenger (**Figure S7**). Indeed, whereas OH• is expected to oxidize t-BuOH as well as ethanol with fast kinetics[80], we observe a significantly weaker DMPO-alkyl• adduct signal with t-BuOH than with ethanol, which is consistent with the lower reactivity of high-valent iron species toward the former

alcohol[74,81]. Our results thus suggest that a non-hydroxyl species, interpreted as a putative Fe(IV) species, could be produced upon oxygenation of natural alluvial soil samples, which calls for further examination of the role of Fe(II)-bearing phases in this process, as discussed in the next section.

Role of the reduced-state iron pool in reactive species production. Addition of ethanol and of phosphate in excess in our experiments conducted with EtOH and phosphate buffer allowed us to compare the soils samples reactivity to air-oxidation on a same basis and to evaluate the role of iron-bearing phases in radical production. Indeed, under this excess phosphate and with the chosen ethanol over DMPO ratio in our experiments, alkyl radicals are mostly produced via the oxidation of ethanol into the α-hydroxyethyl radical by a non-hydroxyl species as indicated by **Figure 2** and illustrated in **Figure S6**, and we interpret these species as Fe(IV) as detailed in the previous section. In **Figure S8**, intensities varied significantly from one replica to another likely because of soils samples heterogeneity, as attested by the error bars representing the standard deviation within triplicate results. However, particular samples with lower radical production could be easily distinguished, i.e. those with the lowest iron content: CRD3 0-3 cm, CRG1 14-21 cm and T1S1 24-30 cm (**Table 1**).

Table 3. Kinetics parameters, namely $[DMPO\text{-}alkyl^{\bullet}]_{max}$, k_{prod} and k_{decay} derived from the fitting to Eq.1 (see text) of the time-course evolution of the DMPO-alkyl$^{\bullet}$ scale factor in the air-oxidation experiments conducted in the presence of ethanol and 0.435 M phosphate buffer. Reported kinetic parameters were obtained from the fitting of the average of triplicate experiments to Eq.1, as shown in **Figure S8**. Uncertainties on $[DMPO\text{-}alkyl^{\bullet}]_{max}$ values are reported under bracket for the last digit and include mean quadratic error on triplicates together with fitting uncertainties to Eq 1. Uncertainties on kinetic constants refer to fitting to Eq 1.

DMPO-alkyl•	[DMPO-alkyl•]max µM	[DMPO-alkyl•]max (a.u.) x10^5	k_{prod} (min^{-1})	k_{decay} (min^{-1})	Chi^2 x10^6	*R*
CRD3 0-3 cm	14.5(17)	0.57(7)	0.22(6)	0.023(3)	109.0	0.956
CRD3 3-10 cm	42.5(23)	1.67(9)	0.35(2)	0.0125(3)	16.54	0.998
CRD3 10-20 cm	49.8(20)	1.96(8)	0.277(9)	0.0071(2)	21.37	0.996
CRD3 20-30 cm	64.0(30)	2.52(12)	0.274(2)	0.00985(4)	0.94	0.999
CRG1 8-14 cm	57.6(8)	2.27(3)	0.253(5)	0.0178(2)	8.25	0.999
CRG1 14-21 cm	31.9(8)	1.26(3)	0.24(2)	0.0113(7)	44.93	0.989
CRG1 21-28 cm	68.1(15)	2.68(6)	0.36(2)	0.144(3)	57.78	0.998
CRG1 28-21 cm	66.0(23)	2.60(9)	0.254(3)	0.0170(1)	5.47	0.999
T1S1 0-10 cm	45.7(20)	1.80(8)	0.283(4)	0.00792(9)	2.64	0.999
T1S1 10-15 cm	47.5(26)	1.87(10)	0.16(1)	0.0077(8)	116.0	0.977
T1S1 15-24 cm	42.2(23)	1.66(9)	0.221(5)	0.0051(2)	10.58	0.995
T1S1 24-30 cm	26.8(25)	1.06(10)	0.18(1)	1.06(3)	47.93	0.968

Figure 3a shows the maximal quantity of DMPO-alkyl• adduct, i.e. [DMPO-alkyl•]$_{max}$ (**Table 3, Figure S8**), produced after 2 min air-oxidation of each soil sample as a function of total iron in the sample. Positive correlations are observed for CRD3, CRG1 and T1S1 core samples, but with a lower rate of radical production with respect to total iron for T1S1 compared to CRD3 and CRG1.

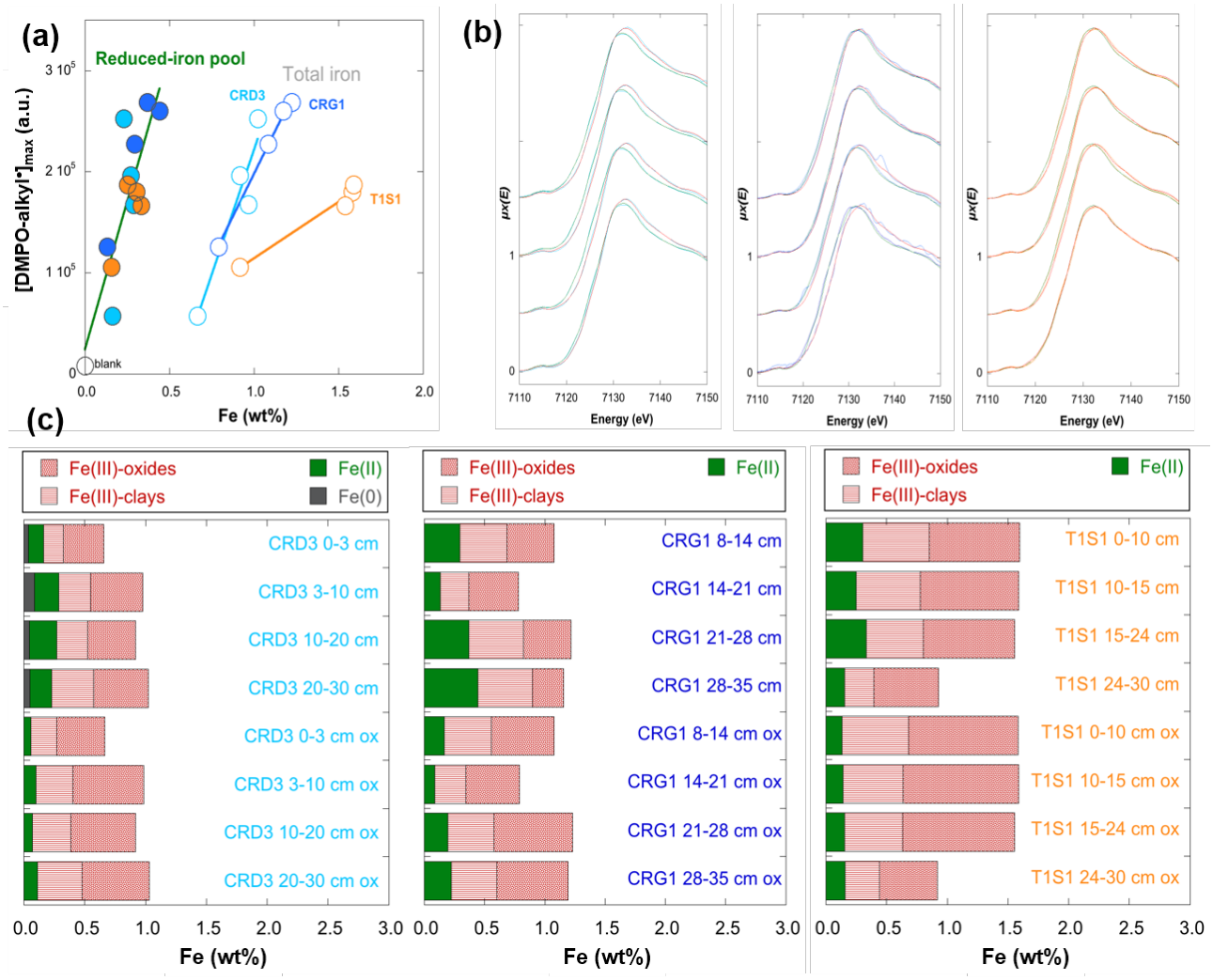

Figure 3. Role of the reduced-state iron pool in reactive species production upon air-oxidation. (a) The quantity of DMPO-alkyl• adduct produced after 2 min air-oxidation is displayed as a function of total iron concentration (open circles) and of the initial reduced-state iron pool (plain circle). Uncertainties fall within the symbol size (**Table 3**). The reduced-state iron pool is calculated as Fe(0)+Fe(II) species in the pristine soil samples, as determined from LCF of XANES data at the Fe K-edge (**Figure 4**; **Table 4**) (b) Detail of the LCF in the edge region is displayed before and after air-oxidation with fit curves displayed as as green and red curves, respectively, and overlap experimental data displayed as light blue, blue and orange colors for CRD3, CRG1 and T1S1, respectively. Strong overlap between fit and experiment relies to fit quality. (c) Iron speciation derived from XANES LCF analysis of the soils core samples before and after 2 min air-oxidation is displayed as bar diagrams scaled to total iron concentration. Additional details on XANES and EXAFS LCF procedures are reported in Supporting Information.

485 Such positive but complex correlation between radical production and total iron content[15] or with
486 Fe(II)[18,20] were previously observed in the past, which emphasizes the need for better identifying the
487 driving factor for radical production, especially using spectroscopic methods[17].
488 In our study, the differences in trend observed between the soils cores when considering total iron
489 may be explained by differences in iron redox state as shown in **Figure 3b and 3c.** Indeed, the energy-
490 shift of the Fe *K*-edge position before and after air-oxidation, is larger for most of the CRD3 and
491 CRG1 samples than for the T1S1 ones (**Figure 3b**). This difference suggests that a larger proportion
492 of total iron has been oxidized upon oxygenation in CRD3 and CRG1 than in T1S1. Accordingly, in
493 the pristine samples, the proportion of initially reduced-state iron species over total iron is higher in
494 CRD3 and CRG1 than in T1S1, as determined from LCF of Fe *K*-edge XANES data (**Table 4**).
495 Hence, when scaling XANES LCF results (**Table 4**) to total iron (**Table 1**), the absolute "reduced-
496 state iron" pool concentration in the pristine soil samples, i.e. Fe(0) + Fe(II) in CRD3 or Fe(II) in
497 T1S1 and CRG1, ranges within similar values for the three soils cores (0.044 – 0.198 wt%) (**Figure**
498 **3c**). It is then possible to compare this reduced-state iron pool in the pristine soil samples with the
499 quantity of radical species produced upon their oxygenation and detected by EPR in the form of
500 DMPO-alkyl$^{\bullet}$ adducts (**Figure 3a**). The differences in radical production trends between the CRD3,
501 CRG1 and T1S1 soils cores tend to vanish when considering the initial reduced-state iron pool instead
502 of total iron. The fast and close-to-linear increase of radical species as a function of reduced-state
503 iron pool (R = 0.85 in **Figure 3a**) could then be interpreted as the initial rate of Fe(IV) production
504 from highly reactive reduced-state Fe species.
505 The identity of the initial reduced-state iron pool species was further investigated by EXAFS LCF
506 (**Figure 4**; **Table 4)**. According to both EXAFS and XANES LCF results, structural Fe(II) in
507 phyllosilicates largely contributed to the oxidizable fraction of iron since it systematically decreased
508 after oxidation (**Figure 3c**; **Table 4)**. Our proxy for the structural-Fe(II) clay component in the
509 XANES and EXAFS LCF analysis is a Fe(II,III) biotite model compound (**Table 4**). Other
510 phyllosilicates may actually host structural-Fe(II) and could match this proxy, especially smectites.

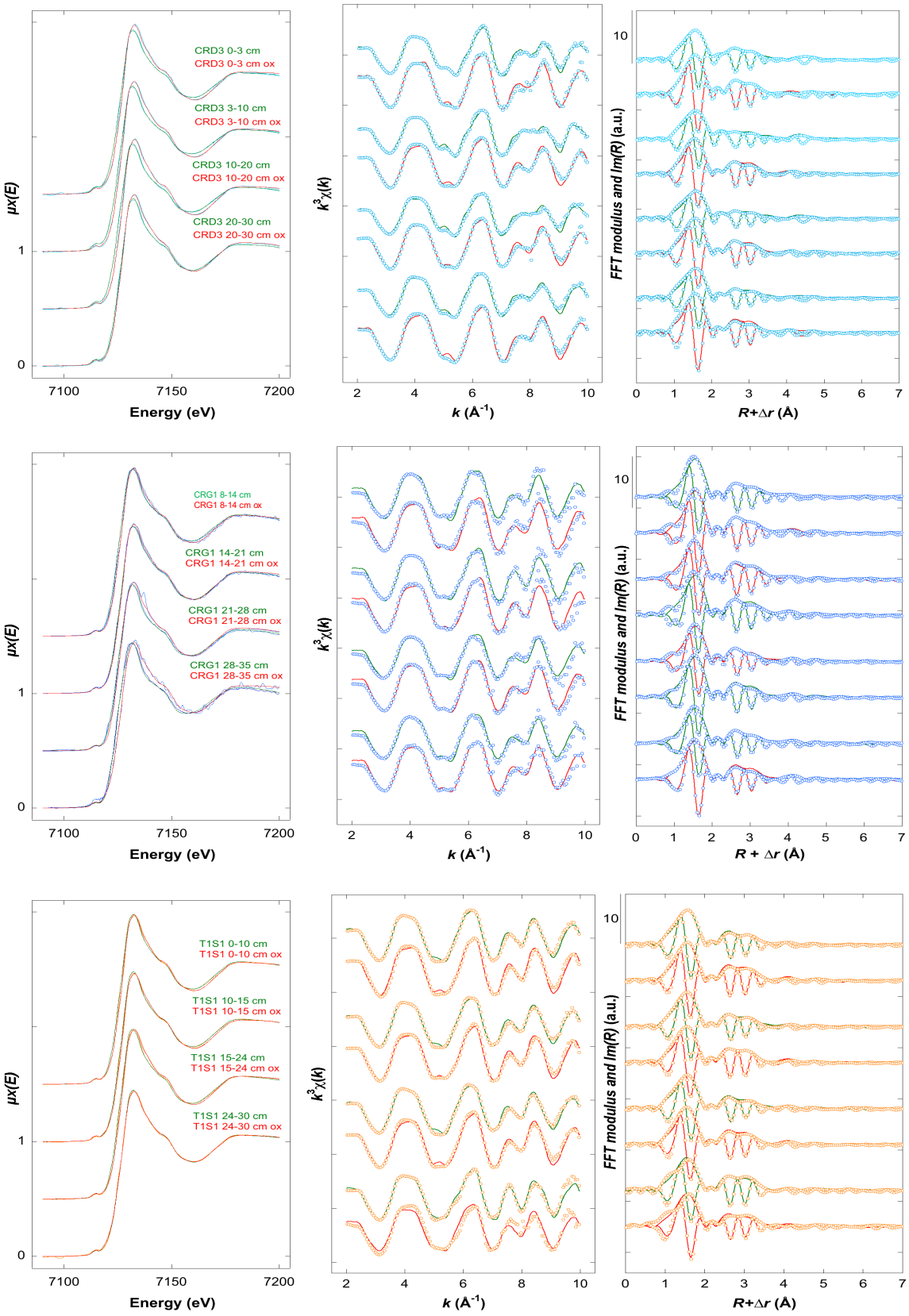

Figure 4. Results of Fe K-edge XANES and EXAFS LCF for all samples studied. Experimental data are plotted in light-blue, blue and orange colours for CRD3, CRG1 and T1S1 core samples, respectively. Fitting curves are plotted in green and red curves for pristine and oxidized samples, respectively

519 **Table 4.** Results of LCF analysis for Fe K-edge XANES and EXAFS data of alluvial soil samples from the
520 Avenelles (CRD3 and CRG1 cores) and upstream-Bassée (T1S1 core) sites, before and after 2 min air-
521 oxidation. Uncertainties on the last digit of reported component proportions are indicated under bracket to
522 99.7% and 95% confidence (3σ and 2σ) for XANES and EXAFS, respectively (see text). Fit quality was
523 estimated by a R factor (Rf) and a reduced χ^2 (chi^2_R)(see text). The proportion of "reduced-state Fe" over total
524 iron is calculated as Fe(0)-metal + Fe(II)-pyrite + Fe(II)-vivianite + 0.7 x Fe(II,III)-biotite, based on the Fe-
525 redox composition of our Fe(II,III)-biotite model compound (**Figure S9**).

XANES LCF Samples	Fe(0)-metal (%)	Fe(II)-pyrite (%)	Fe(II)-vivianite (%)	Fe(II,III)-biotite (%)	Fe(III)-illite (%)	Fe(III)-goethite (%)	*Sum* (%)	*"reduced-state Fe"* (%)	*Rf x10⁴*	*chi^2_R x10³*
CRD3 0-3 cm	6(2)	3(2)	7(2)	12(3)	21(5)	50(5)	100	24(2)	0.25	0.254
CRD3 0-3 cm ox	-	6(2)	-	4(3)	31(10)	59(10)	100	9(2)	1.06	1.077
CRD3 3-10 cm	9(1)	-	9(2)	17(3)	22(5)	44(5)	101	30(2)	0.27	0.270
CRD3 3-10 cm ox	-	3(1)	4(3)	5(5)	30(8)	60(8)	100	11(4)	0.63	0.641
CRD3 10-20 cm	5(2)	2(2)	10(2)	18(3)	22(5)	43(5)	100	30(2)	0.27	0.271
CRD3 10-20 cm ox	-	4(2)	4(1)	-	34(9)	58(9)	100	8(2)	0.76	0.757
CRD3 20-30 cm	5(1)	-	7(2)	15(3)	29(5)	44(5)	100	23(3)	0.27	0.271
CRD3 20-30 cm ox	-	2(2)	5(3)	6(5)	34(9)	54(9)	101	11(5)	0.75	0.774
CRG1 10-14 cm	-	-	13(3)	20(6)	30(10)	36(10)	99	27(5)	1.10	1.091
CRG1 10-14 cm ox	-	-	9(4)	9(7)	33(11)	48(10)	99	15(6)	1.16	1.147
CRG1 14-21 cm	-	1(1)	8(3)	11(5)	27(8)	52(7)	99	17(4)	0.57	0.563
CRG1 14-21 cm ox	-	2(2)	5(3)	6(5)	31(9)	56(9)	100	11(4)	0.76	0.767
CRG1 21-28 cm	-	2(2)	12(3)	23(6)	30(10)	32(10)	99	30(5)	0.95	0.942
CRG1 21-28 cm ox	-	-	16(2)	-	31(20)	53(19)	101	16(2)	4.13	4.128
CRG1 28-35 cm	-	-	18(5)	28(9)	30(15)	22(15)	99	38(8)	2.36	2.313
CRG1 28-35 cm ox	-	8(3)	11(2)	-	32(16)	50(16)	101	19(3)	2.64	2.660
T1S1 0-10 cm	-	1(1)	7(2)	16(3)	30(5)	47(5)	100	19(3)	0.23	0.229
T1S1 0-10 cm ox	-	2(1)	3(2)	5(4)	33(7)	57(7)	100	9(3)	0.46	0.461
T1S1 10-15 cm	-	1(1)	5(2)	14(4)	29(6)	51(6)	100	16(3)	0.33	0.337
T1S1 10-15 cm ox	-	4(1)	5(1)	-	31(7)	60(7)	100	9(1)	0.51	0.506
T1S1 15-24 cm	-	-	9(2)	18(3)	25(5)	49(5)	100	22(6)	0.28	0.281
T1S1 15-24 cm ox	-	2(1)	8(3)	-	31(8)	60(8)	101	10(2)	0.64	0.651
T1S1 24-30 cm	-	5(1)	5(2)	10(4)	23(7)	58(7)	99	17(4)	0.45	0.443
T1S1 24-30 cm ox	-	7(2)	6(3)	6(5)	29(9)	52(8)	99	17(4)	0.73	0.727

EXAFS data Samples	Fe(0)-metal (%)	Fe(II)-pyrite (%)	Fe(II)-vivianite (%)	Fe(II,III)-biotite (%)	Fe(III)-illite (%)	Fe(III)-goethite (%)	*Sum* (%)	*"reduced-state Fe"* (%)	*Rf x10²*	*chi^2_R*
CRD3 0-3 cm	5(2)	-	-	21(11)	30(12)	36(10)	91	20(7)	2.02	2.529
CRD3 0-3 cm ox	2(1)	-	-	-	69(8)	23(8)	94	2(1)	2.66	1.893
CRD3 3-10 cm	7(3)	-	-	33(16)	23(17)	31(14)	94	30(12)	2.55	5.119
CRD3 3-10 cm ox	-	-	-	-	56(19)	26(20)	82	0	3.17	11.80
CRD3 10-20 cm	5(3)	-	-	32(20)	27(21)	27(18)	90	27(15)	3.39	7.607
CRD3 10-20 cm ox	-	-	-	12(10)	52(11)	27(9)	92	8(6)	2.79	2.177
CRD3 20-30 cm	3(4)	-	-	30(24)	35(25)	24(22)	92	24(20)	3.00	11.59
CRD3 20-30 cm ox	3(3)	-	-	-	66(16)	24(17)	93	3(3)	3.41	8.339
CRG1 10-14 cm	-	-	-	25(15)	56(16)	19(13)	100	18(12)	7.93	4.682
CRG1 10-14 cm ox	-	-	-	-	73(13)	20(13)	93	0	6.61	5.427
CRG1 14-21 cm	-	-	-	19(11)	44(11)	39(9)	102	13(8)	5.63	2.330
CRG1 14-21 cm ox	-	-	-	-	59(12)	33(12)	92	0	9.93	4.415
CRG1 21-28 cm	-	-	-	21(19)	52(19)	17(16)	90	15(14)	7.60	7.033
CRG1 21-28 cm ox	-	-	-	13(9)	60(10)	23(8)	94	9(6)	4.76	1.703
CRG1 28-35 cm	-	-	-	27(12)	51(12)	17(10)	95	19(9)	6.07	2.721
CRG1 28-35 cm ox	-	-	-	13(9)	60(10)	23(8)	94	9(6)	4.76	1.703
T1S1 0-10 cm	-	-	-	31(20)	38(20)	31(17)	100	22(16)	2.15	7.645
T1S1 0-10 cm ox	-	-	-	-	54(20)	36(21)	90	0	2.64	13.62
T1S1 10-15 cm	-	-	-	27(13)	40(13)	29(11)	95	19(9)	1.85	3.138
T1S1 10-15 cm ox	-	-	-	-	52(16)	34(16)	85	0	2.44	8.409
T1S1 15-24 cm	-	-	-	33(12)	36(12)	27(10)	97	23(8)	2.41	11.37
T1S1 15-24 cm ox	-	-	-	-	58(18)	28(18)	86	0	2.67	10.51
T1S1 24-30 cm	-	-	-	27(18)	22(19)	49(16)	98	19(13)	4.36	6.779
T1S1 24-30 cm ox	-	-	-	20(18)	40(19)	27(16)	87	14(13)	10.3	6.555

526

This result is in line with other studies[15,17] proposing the Fe(II)-clay component as a major contributor to radical species production upon oxygenation of soils or sediments. In addition, our results suggest that Fe(0), likely from anthropogenic origin (**Figure 1e**), could also contribute to the oxidizable Fe fraction in the CRD3 samples since its proportion systematically decreases after oxidation (**Figure 3c; Table 5.)**. Vivianite (**Figure 1c**) could also contribute to oxidizable iron as indicated by a decrease of this component after air-oxidation **(Table 4)**.

Alternative XANES and/or EXAFS LCF fit solutions could also be obtained, from sample to sample, by adding Fe(II)-polyphosphate or carboxylates fitting components, but with larger uncertainties (data not shown) than in **Table 4**, and resulted however in similar overall Fe(II)-pool quantities. Nevertheless, sorbed- or organic-Fe(II) species could also contribute to the Fe(II) pool and to radical production, as proposed in previous studies[15,23,82,83]. Because of such uncertainties on the identity of minor Fe(II) components, we have chosen in the present study to merge the Fe(II) components in the whole reduced-state iron pool, this latter estimate being accurately estimated by XANES LCF (**Table 3; Figure 3b and Figure 4**), and appearing relevant to be compared with the radical species production rate (**Figure 3a**). Finally, XANES LCF results do not reveal significant pyrite oxidation considering our experimental conditions, which is consistent with the results of previous laboratory experiments conducted under similar oxygenation conditions[36].

Our results thus confirm that iron minerals are susceptible to play a major role in producing reactive species upon soil or sediment oxygenation[15,17]. For instance, a non-linear but positive correlation has been reported[15] between total iron content in river sediments and the amount of $OH^{\bullet}$ produced upon oxygenation, as measured by BA/*p*-HBA method. In the same study, radical species production was found to increase with sediment sampling depth and after their reduction, thus suggesting that Fe(II) may be a major substrate for radical production. Structural and sorbed Fe(II) associated to clay minerals has been proposed as main contributors to radical production upon oxygenation, based on comparative air-oxidation experiments after selective chemical treatments[15], and more recently using spectroscopic analyses[17,39]. Natural organic matter has been also proposed

553 to contribute in other studies[18,24,25,33,84]. The generation of re-oxidizable Fe(II) species in soils is
554 typically attributed to microbial reduction of Fe(III)-minerals under anaerobic flooding conditions[23–
555 25], as those characterizing the alluvial soils studied here.

556 Beyond these previous findings, the present study show that Fe(II)-minerals, especially Fe(II)-
557 bearing phyllosilicates play a key role in the production of non-hydroxyl reactive species in air-
558 oxidation of riverbank soils. We also show that soil sourced and added phosphate favor these non-
559 hydroxyl reactive species over $OH^{\bullet}$ and that natural organic matter may be oxidized by these non-
560 hydroxyl reactive species to form alkyl$^{\bullet}$ and $CO_2^{\bullet-}$ radical species.

561

562 **CONCLUSION**

563 Our results confirm that ferrous iron oxidation can be a major driver for the production of reactive
564 species in soils and sediments upon air-oxidation[15,17,23,82], which is actually recognized as a
565 widespread process that may occur for instance in alluvial plains and coastal areas[18,24,82,85]. However,
566 the identity of the various reactive species produced during iron-bearing minerals oxygenation may
567 vary as a function of physicochemical conditions and are still a matter of research[4,5,34,35,51,77,78]. While
568 it is widely assumed in the literature that OH• is produced, here we show by EPR spin-trapping
569 analysis that another non-hydroxyl species is significantly produced upon air-oxidation of natural
570 soils and sediments. Based on its differential reactivity toward tert-butanol and ethanol, and its
571 enhancement by phosphate ligands, we hypothesize that this non-hydroxyl species could be
572 interpreted as Fe(IV)[4,34–36,65,69,70]. Interestingly, the results of our air-oxidation experiments
573 conducted without phosphate buffer show that this putative Fe(IV) species can be formed in natural
574 soils suspensions, which could be explained by the presence of natural ligands favoring Fe(IV)
575 formation in the soils, especially phosphate.

576

577

ASSOCIATED CONTENT

The supporting information file contains 4 tables (**Tables S1-S4**) and 12 figures (**Figure S1-S12**) including in particular XRD data, kinetics results on reactive species as derived from EPR data fitting, as well as PCA-TT analysis of Fe *K*-edge XANES and EXAFS data.

ACKNOWLEDGMENT

The authors thank Ludovic Delbes and Benoît Baptiste for their help on the XRD platform of IMPMC and Fériel Skouri and Cynthia Travers for their help in the IMPMC chemistry laboratories. Cédric Plessis, Sébastien Breuil and Adrien Lescoat are thanked for their determination of total and organic carbon in soil and aqueous solutions; as well as Eric Vachet and Amélie Trouvé for complementary phosphorus analysis in solutions (Ecosys, INRAE). The ELETTRA synchrotron (Trieste) and SOLEIL synchrotron (Orsay) are acknowledged for having provided beamtime and the authors are especially indebted to Camille Rivard, Delphine Vantelon (LUCIA Beamline at SOLEIL) and Luca Olivi (XAFS Beamline at ELETTRA) for beamline tuning and help during data collection. We thank the SEM-FIB platform staff members of IMPMC, Imène Estève, Béatrice Boisneau, and Stéphanie Delbrel for their help and for providing time on their equipment. The authors are indebted to Xavier Carrier for his help within the framework of the DEPOLECO program. TOC crystallographic structure has been drawn using CrystalMaker®. This study has been granted by ANR DEPOLECO and PIREN Seine research programs.

REFERENCES

(1) Dong, H.; Zeng, G.; Tang, L.; Fan, C.; Zhang, C.; He, X.; He, Y. An Overview on Limitations of TiO2-Based Particles for Photocatalytic Degradation of Organic Pollutants and the Corresponding Countermeasures. *Water Res.* **2015**, *79*, 128–146. https://doi.org/10.1016/j.watres.2015.04.038.

(2) Guan, X.; Sun, Y.; Qin, H.; Li, J.; Lo, I. M. C.; He, D.; Dong, H. The Limitations of Applying Zero-Valent Iron Technology in Contaminants Sequestration and the Corresponding Countermeasures: The Development in Zero-Valent Iron Technology in the Last Two Decades (1994–2014). *Water Res.* **2015**, *75*, 224–248. https://doi.org/10.1016/j.watres.2015.02.034.
(3) Nidheesh, P. V. Heterogeneous Fenton Catalysts for the Abatement of Organic Pollutants from Aqueous Solution: A Review. *RSC Adv.* **2015**, *5* (51), 40552–40577. https://doi.org/10.1039/C5RA02023A.
(4) Keenan, C. R.; Sedlak, D. L. Factors Affecting the Yield of Oxidants from the Reaction of Nanoparticulate Zero-Valent Iron and Oxygen. *Environ. Sci. Technol.* **2008**, *42* (4), 1262–1267. https://doi.org/10.1021/es7025664.
(5) Lee, C. Oxidation of Organic Contaminants in Water by Iron-Induced Oxygen Activation: A Short Review. *Environ. Eng. Res.* **2015**, *20* (3), 205–211. https://doi.org/10.4491/eer.2015.051.
(6) Feitz, A. J.; Joo, S. H.; Guan, J.; Sun, Q.; Sedlak, D. L.; David Waite, T. Oxidative Transformation of Contaminants Using Colloidal Zero-Valent Iron. *Colloids Surf. A: Physicochem. Eng. Asp.* **2005**, *265* (1–3), 88–94. https://doi.org/10.1016/j.colsurfa.2005.01.038.
(7) Fang, G.-D.; Zhou, D.-M.; Dionysiou, D. D. Superoxide Mediated Production of Hydroxyl Radicals by Magnetite Nanoparticles: Demonstration in the Degradation of 2-Chlorobiphenyl. *J. Hazard. Mater.* **2013**, *250–251*, 68–75. https://doi.org/10.1016/j.jhazmat.2013.01.054.
(8) Ardo, S. G.; Nélieu, S.; Ona-Nguema, G.; Delarue, G.; Brest, J.; Pironin, E.; Morin, G. Oxidative Degradation of Nalidixic Acid by Nano-Magnetite via Fe^{2+} /O_2 -Mediated Reactions. *Environ. Sci. Technol.* **2015**, *49* (7), 4506–4514. https://doi.org/10.1021/es505649d.
(9) Cheng, D.; Neumann, A.; Yuan, S.; Liao, W.; Qian, A. Oxidative Degradation of Organic Contaminants by FeS in the Presence of O2. *Environ. Sci. Technol.* **2020**, *54* (7), 4091–4101. https://doi.org/10.1021/acs.est.9b07012.
(10) You, X.; Liu, S.; Berns-Herrboldt, E. C.; Dai, C.; Werth, C. J. Kinetics of Hydroxyl Radical Production from Oxygenation of Reduced Iron Minerals and Their Reactivity with Trichloroethene: Effects of Iron Amounts, Iron Species, and Sulfate Reducing Bacteria. *Environ. Sci. Technol.* **2023**, *57* (12), 4892–4904. https://doi.org/10.1021/acs.est.3c00122.
(11) Zhang, P.; Yuan, S. Production of Hydroxyl Radicals from Abiotic Oxidation of Pyrite by Oxygen under Circumneutral Conditions in the Presence of Low-Molecular-Weight Organic Acids. *Geochim. Cosmochim. Acta* **2017**, *218*, 153–166. https://doi.org/10.1016/j.gca.2017.08.032.
(12) Zeng, Q.; Dong, H.; Wang, X.; Yu, T.; Cui, W. Degradation of 1, 4-Dioxane by Hydroxyl Radicals Produced from Clay Minerals. *Journal of Hazardous Materials* **2017**, *331*, 88–98. https://doi.org/10.1016/j.jhazmat.2017.01.040.
(13) Chen, N.; Fang, G.; Liu, G.; Zhou, D.; Gao, J.; Gu, C. The Degradation of Diethyl Phthalate by Reduced Smectite Clays and Dissolved Oxygen. *Chem. Eng. J.* **2019**, *355*, 247–254. https://doi.org/10.1016/j.cej.2018.08.160.
(14) Huang, L.; Liu, Z.; Dong, H.; Yu, T.; Jiang, H.; Peng, Y.; Shi, L. Coupling Quinoline Degradation with Fe Redox in Clay Minerals: A Strategy Integrating Biological and Physicochemical Processes. *Appl. Clay Sci.* **2020**, *188*, 105504. https://doi.org/10.1016/j.clay.2020.105504.
(15) Tong, M.; Yuan, S.; Ma, S.; Jin, M.; Liu, D.; Cheng, D.; Liu, X.; Gan, Y.; Wang, Y. Production of Abundant Hydroxyl Radicals from Oxygenation of Subsurface Sediments. *Environ. Sci. Technol.* **2016**, *50* (1), 214–221. https://doi.org/10.1021/acs.est.5b04323.
(16) Schaefer, C. E.; Ho, P.; Berns, E.; Werth, C. Mechanisms for Abiotic Dechlorination of Trichloroethene by Ferrous Minerals under Oxic and Anoxic Conditions in Natural Sediments. *Environ. Sci. Technol.* **2018**, *52* (23), 13747–13755. https://doi.org/10.1021/acs.est.8b04108.
(17) Xie, W.; Yuan, S.; Tong, M.; Ma, S.; Liao, W.; Zhang, N.; Chen, C. Contaminant Degradation by •OH during Sediment Oxygenation: Dependence on Fe(II) Species. *Environ. Sci. Technol.* **2020**, *54* (5), 2975–2984. https://doi.org/10.1021/acs.est.9b04870.

(18) Page, S. E.; Kling, G. W.; Sander, M.; Harrold, K. H.; Logan, J. R.; McNeill, K.; Cory, R. M. Dark Formation of Hydroxyl Radical in Arctic Soil and Surface Waters. *Environ. Sci. Technol.* **2013**, *47* (22), 12860–12867. https://doi.org/10.1021/es4033265.
(19) Trusiak, A.; Treibergs, L. A.; Kling, G. W.; Cory, R. M. The Role of Iron and Reactive Oxygen Species in the Production of CO2 in Arctic Soil Waters. *Geochim. Cosmochim. Acta* **2018**, *224*, 80–95. https://doi.org/10.1016/j.gca.2017.12.022.
(20) Liao, P.; Yu, K.; Lu, Y.; Wang, P.; Liang, Y.; Shi, Z. Extensive Dark Production of Hydroxyl Radicals from Oxygenation of Polluted River Sediments. *Chem. Eng. J.* **2019**, *368*, 700–709. https://doi.org/10.1016/j.cej.2019.03.018.
(21) Chen, Y.; Miller, C. J.; Waite, T. D. Heterogeneous Fenton Chemistry Revisited: Mechanistic Insights from Ferrihydrite-Mediated Oxidation of Formate and Oxalate. *Environ. Sci. Technol.* **2021**, *55* (21), 14414–14425. https://doi.org/10.1021/acs.est.1c00284.
(22) Yu, C.; Lu, Y.; Zhang, Y.; Qian, A.; Zhang, P.; Tong, M.; Yuan, S. Significant Contribution of Solid Organic Matter for Hydroxyl Radical Production during Oxygenation. *Environ. Sci. Technol.* **2022**, *56* (16), 11878–11887. https://doi.org/10.1021/acs.est.2c02766.
(23) Zhao, G.; Tan, M.; Wu, B.; Zheng, X.; Xiong, R.; Chen, B.; Kappler, A.; Chu, C. Redox Oscillations Activate Thermodynamically Stable Iron Minerals for Enhanced Reactive Oxygen Species Production. *Environ. Sci. Technol.* **2023**, *57* (23), 8628–8637. https://doi.org/10.1021/acs.est.3c02302.
(24) Du, H.; Cao, Y.; Li, Z.; Li, L.; Xu, H. Formation and Mechanisms of Hydroxyl Radicals during the Oxygenation of Sediments in Lake Poyang, China. *Water Res.* **2021**, *202*, 117442. https://doi.org/10.1016/j.watres.2021.117442.
(25) Du, H.; Wang, H.; Chi, Z.; Song, N.; Wang, C.; Xu, H. Burst of Hydroxyl Radicals in Sediments Derived by Flooding/Drought Transformation Process in Lake Poyang, China. *Sci. Total Environ.* **2021**, *772*, 145059. https://doi.org/10.1016/j.scitotenv.2021.145059.
(26) Wang, Y.; Huang, D.; Ge, C.; Wang, X.; Zhu, C.; Chen, N.; Fang, G.; Zhou, D. Amendment of Organic Acids Significantly Enhanced Hydroxyl Radical Production during Oxygenation of Paddy Soils. *J. Hazard. Mater.* **2023**, *457*, 131799. https://doi.org/10.1016/j.jhazmat.2023.131799.
(27) Pryor, W. A. Oxy-Radicals and Related Species: Their Formation, Lifetimes, and Reactions. *Annu. Rev. Physiol.* **1986**, *48* (1), 657–667. https://doi.org/10.1146/annurev.ph.48.030186.003301.
(28) Zhou, X.; Mopper, K. Determination of Photochemically Produced Hydroxyl Radicals in Seawater and Freshwater. *Mar. Chem.* **1990**, *30*, 71–88. https://doi.org/10.1016/0304-4203(90)90062-H.
(29) Xie, W.; Zhang, P.; Liao, W.; Tong, M.; Yuan, S. Ligand-Enhanced Electron Utilization for Trichloroethylene Degradation by ˙OH during Sediment Oxygenation. *Environ. Sci. Technol.* **2021**, *55* (10), 7044–7051. https://doi.org/10.1021/acs.est.1c00136.
(30) Zhang, P.; Liu, J.; Yu, H.; Cheng, D.; Liu, H.; Yuan, S. Kinetic Models for Hydroxyl Radical Production and Contaminant Removal during Soil/Sediment Oxygenation. *Water Res.* **2023**, *240*, 120071. https://doi.org/10.1016/j.watres.2023.120071.
(31) He, J.; Miller, C. J.; Collins, R.; Wang, D.; Waite, T. D. Production of a Surface-Localized Oxidant during Oxygenation of Mackinawite (FeS). *Environ. Sci. Technol.* **2020**, *54* (2), 1167–1176. https://doi.org/10.1021/acs.est.9b03975.
(32) Li, K.; Ma, S.; Zou, C.; Latif, J.; Jiang, Y.; Ni, Z.; Shen, S.; Feng, J.; Jia, H. Unrecognized Role of Organic Acid in Natural Attenuation of Pollutants by Mackinawite (FeS): The Significance of Carbon-Center Free Radicals. *Environ. Sci. Technol.* **2023**, *57* (49), 20871–20880. https://doi.org/10.1021/acs.est.3c07473.
(33) Liu, F.; Wang, Z.; Liu, J.; Latif, J.; Qin, J.; Yang, H.; Jiang, W.; Deng, Y.; Yang, K.; Ni, Z.; Ding, Y.; Xie, J.; Wang, Y.; Jia, H. Seasonal and Spatial Fluctuations of Reactive Oxygen Species in Riparian Soils and Their Contributions on Organic Carbon Mineralization. *Environ. Sci. Technol.* **2024**, *58* (16), 7066–7077. https://doi.org/10.1021/acs.est.3c10756.

(34) Reinke, L. A.; Rau, J. M.; McCay, P. B. Characteristics of an Oxidant Formed during Iron (II) Autoxidation. *Free Radic. Biol. and Med.* **1994**, *16* (4), 485–492. https://doi.org/10.1016/0891-5849(94)90126-0.
(35) Welch, K. D.; Davis, T. Z.; Aust, S. D. Iron Autoxidation and Free Radical Generation: Effects of Buffers, Ligands, and Chelators. *Arch. of Biochem. Biophys.* **2002**, *397* (2), 360–369. https://doi.org/10.1006/abbi.2001.2694.
(36) Morin, G.; Averseng, F.; Carrier, X.; Le Pape, P.; Du, Y.; HongE, Y.; Bourbon, E.; Sportelli, G.; Da Silva, T. A.; Mezzetti, A.; Baya, C.; Allard, T.; Brest, J.; Rouelle, M. Phosphate Boosts Nonhydroxyl Radical Species Production upon Air Oxidation of Magnetite and Iron Sulfides at Neutral pH. *J. Phys. Chem. C* **2023**, *127* (20), 9650–9662. https://doi.org/10.1021/acs.jpcc.3c02236.
(37) Zong, Y.; Mao, Y.; Xu, L.; Wu, D. Non-Selective Degradation of Organic Pollutants via Dioxygen Activation Induced by Fe(II)-Tetrapolyphosphate Complexes: Identification of Reactive Oxidant and Kinetic Modeling. *Chem. Eng. J.* **2020**, *398*, 125603. https://doi.org/10.1016/j.cej.2020.125603.
(38) Zhang, C.; Kong, C.; Tratnyek, P. G.; Qin, C.; Zhao, Y.; Piao, Y. Effect of Interfacial Action on the Generation and Transformation of Reactive Oxygen Species in Tripolyphosphate-Enhanced Heterogeneous Fe3O4/O2 Systems. *Environ. Sci. Technol.* **2024**, *58* (2), 1378–1389. https://doi.org/10.1021/acs.est.3c07372.
(39) Guo, D.; Xia, Q.; Zeng, Q.; Wang, X.; Dong, H. Antibacterial Mechanisms of Reduced Iron-Containing Smectite–Illite Clay Minerals. *Environ. Sci. Technol.* **2021**, *55* (22), 15256–15265. https://doi.org/10.1021/acs.est.1c04367.
(40) Chen, Y.; Miller, C. J.; Xie, J.; Waite, T. D. Challenges Relating to the Quantification of Ferryl(IV) Ion and Hydroxyl Radical Generation Rates Using Methyl Phenyl Sulfoxide (PMSO), Phthalhydrazide, and Benzoic Acid as Probe Compounds in the Homogeneous Fenton Reaction. *Environ. Sci. Technol.* **2023**, acs.est.2c06753. https://doi.org/10.1021/acs.est.2c06753.
(41) Gu, A. Y.; Musgrave, C.; Goddard, W. A.; Hoffmann, M. R.; Colussi, A. J. Role of Ferryl Ion Intermediates in Fast Fenton Chemistry on Aqueous Microdroplets. *Environ. Sci. Technol.* **2021**, *55* (21), 14370–14377. https://doi.org/10.1021/acs.est.1c01962.
(42) Liang, J.; Duan, X.; Xu, X.; Chen, K.; Zhang, Y.; Zhao, L.; Qiu, H.; Wang, S.; Cao, X. Persulfate Oxidation of Sulfamethoxazole by Magnetic Iron-Char Composites via Nonradical Pathways: Fe(IV) Versus Surface-Mediated Electron Transfer. *Environ. Sci. Technol.* **2021**, *55* (14), 10077–10086. https://doi.org/10.1021/acs.est.1c01618.
(43) England, J.; Martinho, M.; Farquhar, E. R.; Frisch, J. R.; Bominaar, E. L.; Münck, E.; Que, L. A Synthetic High-Spin Oxoiron(IV) Complex: Generation, Spectroscopic Characterization, and Reactivity. *Angew. Chem. Int. Ed.* **2009**, *48* (20), 3622–3626. https://doi.org/10.1002/anie.200900863.
(44) Wan, D.; Liu, F.-F.; Chen, J.-B.; Kappler, A.; Kuzyakov, Y.; Liu, C.-Q.; Yu, G.-H. Microbial Community Mediates Hydroxyl Radical Production in Soil Slurries by Iron Redox Transformation. *Water Res.* **2022**, *220*, 118689. https://doi.org/10.1016/j.watres.2022.118689.
(45) Seder-Colomina, M.; Mangeret, A.; Bauda, P.; Brest, J.; Stetten, L.; Merrot, P.; Julien, A.; Diez, O.; Barker, E.; Billoir, E.; Poupin, P.; Thouvenot, A.; Cazala, C.; Morin, G. Influence of Microorganisms on Uranium Release from Mining-Impacted Lake Sediments under Various Oxygenation Conditions. *Environ. Sci.: Processes Impacts* **2022**, *24* (10), 1830–1843. https://doi.org/10.1039/D2EM00104G.
(46) Harris, D.; Horwáth, W. R.; van Kessel, C. Acid Fumigation of Soils to Remove Carbonates Prior to Total Organic Carbon or CARBON-13 Isotopic Analysis. *Soil Sci. Soc. Am. J.* **2001**, *65* (6), 1853–1856. https://doi.org/10.2136/sssaj2001.1853.
(47) Rodier, J.; Legube, B.; Merlet, N. *L'analyse de l'eau Ed. 10*; Dunod, 2016.
(48) Morin, G.; Bonnin, D. Modeling EPR Powder Spectra Using Numerical Diagonalization of the Spin Hamiltonian. *J. Magn. Reson.* **1999**, *136* (2), 176–199. https://doi.org/10.1006/jmre.1998.1615.

(49) Ravel, B.; Newville, M. ATHENA, ARTEMIS, HEPHAESTUS: Data Analysis for X-Ray Absorption Spectroscopy Using IFEFFIT. *J Synchrotron Rad* **2005**, *12* (4), 537–541. https://doi.org/10.1107/S0909049505012719.
(50) Webb, S. M. SIXpack: A Graphical User Interface for XAS Analysis Using IFEFFIT. *Phys. Scr.* **2005**, *2005* (T115), 1011. https://doi.org/10.1238/Physica.Topical.115a01011.
(51) Morin, G.; Juillot, F.; Casiot, C.; Bruneel, O.; Personné, J.-C.; Elbaz-Poulichet, F.; Leblanc, M.; Ildefonse, P.; Calas, G. Bacterial Formation of Tooeleite and Mixed Arsenic(III) or Arsenic(V)−Iron(III) Gels in the Carnoulès Acid Mine Drainage, France. A XANES, XRD, and SEM Study. *Environ. Sci. Technol.* **2003**, *37* (9), 1705–1712. https://doi.org/10.1021/es025688p.
(52) Morin, G.; Noël, V.; Menguy, N.; Brest, J.; Baptiste, B.; Tharaud, M.; Ona-Nguema, G.; Ikogou, M.; Viollier, E.; Juillot, F. Nickel Accelerates Pyrite Nucleation at Ambient Temperature. *Geochem. Persp. Let.* **2017**, 6–11. https://doi.org/10.7185/geochemlet.1738.
(53) Noël, V.; Marchand, C.; Juillot, F.; Ona-Nguema, G.; Viollier, E.; Marakovic, G.; Olivi, L.; Delbes, L.; Gelebart, F.; Morin, G. EXAFS Analysis of Iron Cycling in Mangrove Sediments Downstream a Lateritized Ultramafic Watershed (Vavouto Bay, New Caledonia). *Geochim. Cosmochim. Acta* **2014**, *136*, 211–228. https://doi.org/10.1016/j.gca.2014.03.019.
(54) Baya, C.; Le Pape, P.; Baptiste, B.; Brest, J.; Landrot, G.; Elkaim, E.; Noël, V.; Blanchard, M.; Ona-Nguema, G.; Juillot, F.; Morin, G. Influence of Trace Level As or Ni on Pyrite Formation Kinetics at Low Temperature. *Geochim. Cosmochim. Acta* **2021**, *300*, 333–353. https://doi.org/10.1016/j.gca.2021.01.042.
(55) Lefebvre, P.; Le Pape, P.; Mangeret, A.; Gourgiotis, A.; Sabatier, P.; Louvat, P.; Diez, O.; Mathon, O.; Hunault, M. O. J. Y.; Baya, C.; Darricau, L.; Cazala, C.; Bargar, J. R.; Gaillardet, J.; Morin, G. Uranium Sorption to Organic Matter and Long-Term Accumulation in a Pristine Alpine Wetland. *Geochim. Cosmochim. Acta* **2022**, *338*, 322–346. https://doi.org/10.1016/j.gca.2022.10.018.
(56) Krause, M. O.; Oliver, J. H. Natural Widths of Atomic K and L Levels, Kα X-ray Lines and Several KLL Auger Lines. *J. Phys. Chem. Ref. Data* **1979**, *8* (2), 329–338. https://doi.org/10.1063/1.555595.
(57) Merrot, P.; Juillot, F.; Noël, V.; Lefebvre, P.; Brest, J.; Menguy, N.; Guigner, J.-M.; Blondeau, M.; Viollier, E.; Fernandez, J.-M.; Moreton, B.; Bargar, J. R.; Morin, G. Nickel and Iron Partitioning between Clay Minerals, Fe-Oxides and Fe-Sulfides in Lagoon Sediments from New Caledonia. *Science of The Total Environment* **2019**, *689*, 1212–1227. https://doi.org/10.1016/j.scitotenv.2019.06.274.
(58) Stetten, L.; Mangeret, A.; Brest, J.; Seder-Colomina, M.; Le Pape, P.; Ikogou, M.; Zeyen, N.; Thouvenot, A.; Julien, A.; Alcalde, G.; Reyss, J. L.; Bombled, B.; Rabouille, C.; Olivi, L.; Proux, O.; Cazala, C.; Morin, G. Geochemical Control on the Reduction of U(VI) to Mononuclear U(IV) Species in Lacustrine Sediments. *Geochimica et Cosmochimica Acta* **2018**, *222*, 171–186. https://doi.org/10.1016/j.gca.2017.10.026.
(59) Ingall, E. D.; Diaz, J. M.; Longo, A. F.; Oakes, M.; Finney, L.; Vogt, S.; Lai, B.; Yager, P. L.; Twining, B. S.; Brandes, J. A. Role of Biogenic Silica in the Removal of Iron from the Antarctic Seas. *Nat Commun* **2013**, *4* (1), 1981. https://doi.org/10.1038/ncomms2981.
(60) Finkelstein, E.; Rosen, G. M.; Rauckman, E. J. Spin Trapping of Superoxide and Hydroxyl Radical: Practical Aspects. *Arch. of Biochem. Biophys.* **1980**, *200* (1), 1–16. https://doi.org/10.1016/0003-9861(80)90323-9.
(61) Buettner, G. R. Spin Trapping: ESR Parameters If Spin Adducts. *Free Radic. Biol. Med.* **1987**, *3* (4), 259–303. https://doi.org/10.1016/s0891-5849(87)80033-3.
(62) Finkelstein, E.; Rosen, G. M.; Rauckman, E. J. Production of Hydroxyl Radical by Decomposition of Superoxide Spin-Trapped Adducts. *Mol. Pharmacol.* **1982**, *21* (2), 262.
(63) Buettner, G. R.; Oberley, L. W. Considerations in the Spin Trapping of Superoxide and Hydroxyl Radical in Aqueous Systems Using 5,5-Dimethyl-1-Pyrroline-1-Oxide. *Biochem. Biophys. Res. Commun.* **1978**, *83* (1), 69–74. https://doi.org/10.1016/0006-291X(78)90398-4.

(64) Zalma, R.; Bonneau, L.; Guignard, J.; Pezerat, H.; Jaurand, M.-C. Formation of Oxy Radicals by Oxygen Reduction Arising from the Surface Activity of Asbestos. *Can. J. Chem.* **1987**, *65* (10), 2338–2341. https://doi.org/10.1139/v87-390.

(65) Yamazaki, I.; Piette, L. H. EPR Spin-Trapping Study on the Oxidizing Species Formed in the Reaction of the Ferrous Ion with Hydrogen Peroxide. *J. Am. Chem. Soc.* **1991**, *113* (20), 7588–7593. https://doi.org/10.1021/ja00020a021.

(66) Rosso, J. A.; Bertolotti, S. G.; Braun, A. M.; Mártire, D. O.; Gonzalez, M. C. Reactions of Carbon Dioxide Radical Anion with Substituted Benzenes: REACTION OF CO_2 RADICAL CATION WITH BENZENES. *J. Phys. Org. Chem.* **2001**, *14* (5), 300–309. https://doi.org/10.1002/poc.365.

(67) Zhou, Q.; Niu, W.; Li, Y.; Li, X. Photoinduced Fenton-Simulated Reduction System Based on Iron Cycle and Carbon Dioxide Radicals Production for Rapid Removal of Cr(VI) from Wastewater. *J. Clean. Prod.* **2020**, *258*, 120790. https://doi.org/10.1016/j.jclepro.2020.120790.

(68) Buxton, G. V.; Greenstock, C. L.; Helman, W. P.; Ross, A. B. Critical Review of Rate Constants for Reactions of Hydrated Electrons, Hydrogen Atoms and Hydroxyl Radicals (·OH/·O^- in Aqueous Solution. *Journal of Physical and Chemical Reference Data* **1988**, *17* (2), 513–886. https://doi.org/10.1063/1.555805.

(69) Jacobsen, F.; Holcman, J.; Sehested, K. Reactions of the Ferryl Ion with Some Compounds Found in Cloud Water. *Int. J. Chem. Kinet.* **1998**, *30* (3), 215–221. https://doi.org/10.1002/(SICI)1097-4601(1998)30:3<215::AID-KIN7>3.0.CO;2-V.

(70) Pestovsky, O.; Bakac, A. Reactivity of Aqueous Fe(IV) in Hydride and Hydrogen Atom Transfer Reactions. *J. Am. Chem. Soc.* **2004**, *126* (42), 13757–13764. https://doi.org/10.1021/ja0457112.

(71) Bray, W. C.; Gorin, M. H. FERRYL ION, A COMPOUND OF TETRAVALENT IRON. *J. Am. Chem. Soc.* **1932**, *54* (5), 2124–2125. https://doi.org/10.1021/ja01344a505.

(72) Yamazaki, I.; Piette, L. H. ESR Spin-Trapping Studies on the Reaction of Fe2+ Ions with H2O2-Reactive Species in Oxygen Toxicity in Biology. *J. Biol. Chem.* **1990**, *265* (23), 13589–13594. https://doi.org/10.1016/S0021-9258(18)77389-4.

(73) Sawyer, D. T.; Kang, C.; Llobet, A.; Redman, C. Fenton Reagents (1:1 FeIILx/HOOH) React via [LxFeIIOOH(BH+)] (1) as Hydroxylases (RH .Fwdarw. ROH), Not as Generators of Free Hydroxyl Radicals (HO.Bul.). *J. Am. Chem. Soc.* **1993**, *115* (13), 5817–5818. https://doi.org/10.1021/ja00066a057.

(74) Pignatello, J. J.; Liu, D.; Huston, P. Evidence for an Additional Oxidant in the Photoassisted Fenton Reaction. *Environ. Sci. Technol.* **1999**, *33* (11), 1832–1839. https://doi.org/10.1021/es980969b.

(75) Bataineh, H.; Pestovsky, O.; Bakac, A. pH-Induced Mechanistic Changeover from Hydroxyl Radicals to Iron(Iv) in the Fenton Reaction. *Chem. Sci.* **2012**, *3* (5), 1594. https://doi.org/10.1039/c2sc20099f.

(76) Lee, H.; Lee, H.-J.; Sedlak, D. L.; Lee, C. pH-Dependent Reactivity of Oxidants Formed by Iron and Copper-Catalyzed Decomposition of Hydrogen Peroxide. *Chemosphere* **2013**, *92* (6), 652–658. https://doi.org/10.1016/j.chemosphere.2013.01.073.

(77) Hug, S. J.; Leupin, O. Iron-Catalyzed Oxidation of Arsenic(III) by Oxygen and by Hydrogen Peroxide: pH-Dependent Formation of Oxidants in the Fenton Reaction. *Environ. Sci. Technol.* **2003**, *37* (12), 2734–2742. https://doi.org/10.1021/es026208x.

(78) Kim, H.-H.; Lee, H.; Kim, H.-E.; Seo, J.; Hong, S. W.; Lee, J.-Y.; Lee, C. Polyphosphate-Enhanced Production of Reactive Oxidants by Nanoparticulate Zero-Valent Iron and Ferrous Ion in the Presence of Oxygen: Yield and Nature of Oxidants. *Water Res.* **2015**, *86*, 66–73. https://doi.org/10.1016/j.watres.2015.06.016.

(79) Farinelli, G.; Minella, M.; Pazzi, M.; Giannakis, S.; Pulgarin, C.; Vione, D.; Tiraferri, A. Natural Iron Ligands Promote a Metal-Based Oxidation Mechanism for the Fenton Reaction in Water Environments. *J. Hazard. Mater.* **2020**, *393*, 122413. https://doi.org/10.1016/j.jhazmat.2020.122413.

(80) Alam, M. S.; Rao, B. S. M.; Janata, E. OH Reactions with Aliphatic Alcohols: Evaluation of Kinetics by Direct Optical Absorption Measurement. A Pulse Radiolysis Study. *Radiat. Phys. Chem.* **2003**, *67* (6), 723–728. https://doi.org/10.1016/S0969-806X(03)00310-4.
(81) Rahhal, S.; Richter, H. W. Reaction of Hydroxyl Radicals with the Ferrous and Ferric Iron Chelates of Diethylenetriamine-N,N,N′,N″,N″-Pentaacetate. *Free Radic. Res. Commun.* **1989**, *6* (6), 369–377. https://doi.org/10.3109/10715768909087920.
(82) Jia, M.; Bian, X.; Yuan, S. Production of Hydroxyl Radicals from Fe(II) Oxygenation Induced by Groundwater Table Fluctuations in a Sand Column. *Sci. Total Environ.* **2017**, *584–585*, 41–47. https://doi.org/10.1016/j.scitotenv.2017.01.142.
(83) Yu, C.; Lu, Y.; Zhang, Y.; Qian, A.; Zhang, P.; Tong, M.; Yuan, S. Significant Contribution of Solid Organic Matter for Hydroxyl Radical Production during Oxygenation. *Environ. Sci. Technol.* **2022**, *56* (16), 11878–11887. https://doi.org/10.1021/acs.est.2c02766.
(84) Zeng, Q.; Wang, X.; Liu, X.; Huang, L.; Hu, J.; Chu, R.; Tolic, N.; Dong, H. Mutual Interactions between Reduced Fe-Bearing Clay Minerals and Humic Acids under Dark, Oxygenated Conditions: Hydroxyl Radical Generation and Humic Acid Transformation. *Environ. Sci. Technol.* **2020**, *54* (23), 15013–15023. https://doi.org/10.1021/acs.est.0c04463.
(85) Du, H.; Wang, H.; Chi, Z.; Song, N.; Wang, C.; Xu, H. Burst of Hydroxyl Radicals in Sediments Derived by Flooding/Drought Transformation Process in Lake Poyang, China. *Sci. Total Environ.* **2021**, *772*, 145059. https://doi.org/10.1016/j.scitotenv.2021.145059.